

JGR Planets

RESEARCH ARTICLE

10.1029/2024JE008486

Key Points:

- · The Martian crust can partially melt at its base during its formation in presence of a low amount of water and in absence of plate tectonics
- · Partial melting of the crust occurs in thick crust regions such as the highlands, where differentiated rocks
- A non-negligible fraction of evolution scenarios fitting InSight constraints show one or two crustal melting episodes only in the highlands

Correspondence to:

V. Bonnet Gibet, valentin.bonnetgibet@proton.me

Bonnet Gibet, V., Michaut, C., Bodin, T., Wieczorek, M., & Dubuffet, F. (2025). Martian highlands differentiation concomitant to dichotomy formation. Journal of Geophysical Research: Planets, 130, e2024JE008486. https://doi.org/10. 1029/2024JE008486

Received 16 MAY 2024 Accepted 25 FEB 2025

Author Contributions:

Conceptualization: Valentin Bonnet Gibet, Chloé Michaut Data curation: Valentin Bonnet Gibet Formal analysis: Valentin Bonnet Gibet, Chloé Michaut, Thomas Bodin Funding acquisition: Chloé Michaut Investigation: Valentin Bonnet Gibet, Chloé Michaut, Mark Wieczorek Methodology: Valentin Bonnet Gibet, Chloé Michaut, Thomas Bodin Project administration: Chloé Michaut Resources: Chloé Michaut Software: Valentin Bonnet Gibet. Fabien Dubuffet

Mark Wieczorek Visualization: Valentin Bonnet Gibet, Chloé Michaut, Thomas Bodin Writing - original draft: Valentin Bonnet

Supervision: Chloé Michaut.

Gibet

© 2025. The Author(s).

This is an open access article under the terms of the Creative Commons Attribution-NonCommercial-NoDerivs License, which permits use and distribution in any medium, provided the original work is properly cited, the use is non-commercial and no modifications or adaptations are made.

Martian Highlands Differentiation Concomitant to Dichotomy Formation

Valentin Bonnet Gibet^{1,2}, Chloé Michaut^{1,3}, Thomas Bodin^{1,4}, Mark Wieczorek⁵, and Fabien Dubuffet1

¹Ecole Normale Supérieure de Lyon, Université de Lyon, Université Claude Bernard Lyon 1, Université Jean Monet, CNRS, Laboratoire de Géologie de Lyon, Terre, Planètes, Environnement, Lyon, France, ²Institute of Planetary Research, Deutsches Zentrum für Luft- und Raumfahrt, Berlin, Germany, ³Institut Universitaire de France, Paris, France, ⁴Instituto de Ciencias del Mar (ICM) - CSIC, Ciutat Vella, Barcelona, ⁵Institut de Physique du Globe de Paris, Paris, France

Abstract The Martian surface composition appears mainly mafic but recent observations have revealed the presence of differentiated rocks, only in the highlands. Here, we demonstrate that differentiated melts can form during the construction of thick crustal regions on Mars by fractional crystallisation of a mafic magma, without plate tectonics. On a stagnant-lid planet, regions of thicker crusts contain more heat-producing elements and are associated to thinner lithospheres and to higher mantle melt fractions. This induces larger crustal extraction rates where the crust is thicker. This positive feedback mechanism is favored at large wavelengths and can explain the formation of the Martian dichotomy. We further develop an asymmetric parameterized thermal evolution model accounting for crustal extraction, where the well-mixed convective mantle is topped by two lithospheres (north/ south) characterized by specific thermal and crustal structures. We use this model in a Bayesian inversion to investigate the conditions that allow crustal temperatures to be maintained above the basalt solidus during crustal growth, resulting in the formation of evolved melts. Among the thermal evolution models matching constraints on the structure of the Martian crust and mantle provided by the InSight NASA mission, a nonnegligible fraction allows partial melting and differentiation of the crust in the south, which can occur very early (<100 Myr) as well as during the Hesperian; partial melting in the north appears unlikely. Although crustal differentiation may occur on a hemispheric scale on Mars, its vertical extent would be limited to less than a third of the crustal thickness.

Plain Language Summary While the surface of Mars appears mostly mafic, studies using recent observations of differentiated rocks in the highlands of Mars have questioned their origins and significance. Our study proposes that these rocks can form concomitantly to the growth of the crust, by fractional crystallisation of a mafic magma in thick crustal regions. Thicker crusts contain more heat-producing elements, and are associated with hotter lithospheres and increased partial melt fractions in the mantle beneath and hence to faster crustal thickening rates. Temperatures in thicker crustal regions are thus more likely to reach the basalt solidus. By modeling the thermal evolution of Mars, we show that temperatures greater than the basalt solidus can be maintained during the growth of the Martian crust, but only in thick crustal regions, allowing the formation and extraction of differentiated melts. Among the thermal evolution models that are in agreement with the presentday thermal structure of Mars, as revealed by the NASA InSight mission, a significant number allows partial melting in the southern crust, in the very early history of Mars or during the Hesperian. Partial melting of the crust in the north does not seem likely.

1. Introduction

The composition of the Martian crust appears globally basaltic (G. J. Taylor, 2013). Martian meteorites have mafic to ultra-mafic compositions, as do a large proportion of the rocks observed in-situ by rovers. The density of pore-free Martian rocks, or grain density, estimated from their petrology and from surface concentrations in Fe, Al, Ca, Si, and K measured by GRS data, is rather high, between 3,100 and 3,300 kg m⁻³, with potentially lower values in the highlands (Baratoux et al., 2014). Topography and gravity data, on the other hand, suggest lower crustal density values. Pauer and Breuer (2008) constrained the average crustal density of the highlands to values $<3,020 \text{ kg m}^{-3}$ and Goossens et al. (2017) estimated an average density of $2,582 \pm 209 \text{ kg m}^{-3}$ for the crust. Significant lateral density variations may exist between the highlands, where the density could be as low as 1,800-2,000 kg m⁻³, the northern plains, which seems on average denser than the south, and the recent volcanic massifs

BONNET GIBET ET AL. 1 of 31

onlinelibrary.wiley.com/doi/10.1029/2024JE008486 by Dtsch Zentrum F. Luft-U. Raum Fahrt In D. Helmholtz Gemein.,

Writing – review & editing: Valentin Bonnet Gibet, Chloé Michaut, Thomas Bodin

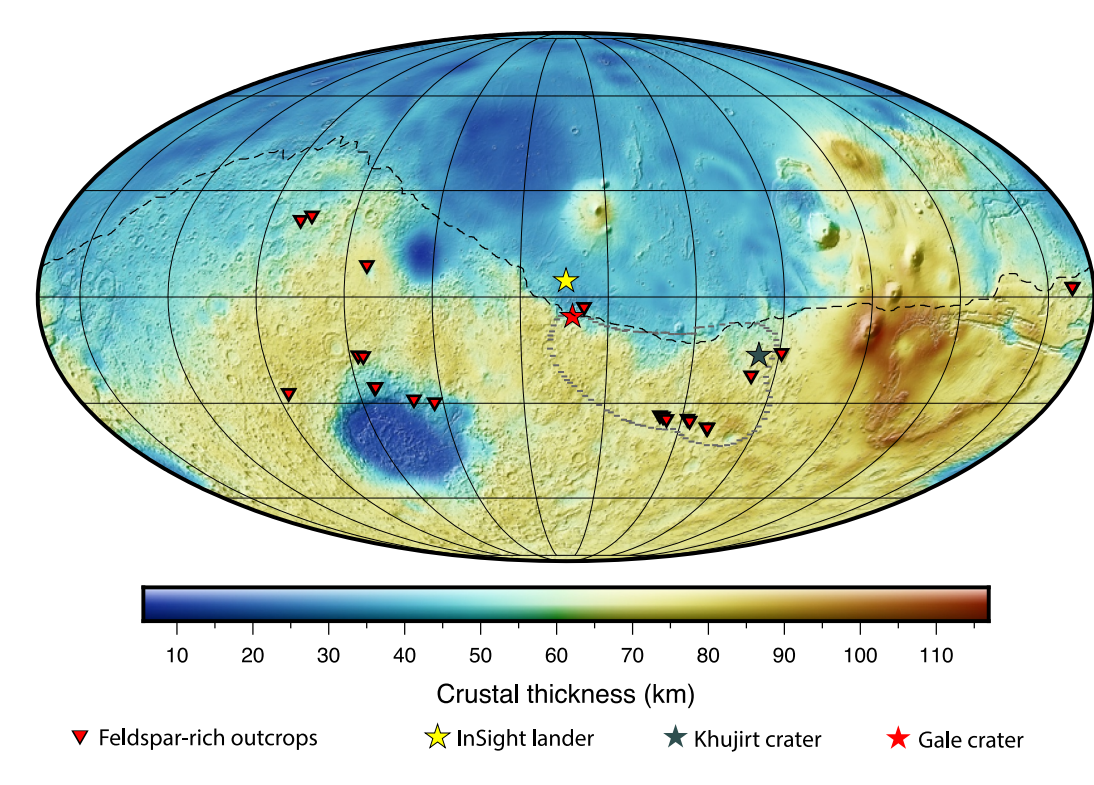


Figure 1. Locations of feldspar-rich and evolved rocks superposed on a crustal thickness map of Mars. This crustal thickness map was built considering a uniform crustal density of 2,900 kg m⁻³, the mantle density model of Khan et al. (2021) and a crustal thickness at the Insight landing site (yellow star) of 39 km (Knapmeyer-Endrun et al., 2021; Wieczorek et al., 2022). This map is presented on a Mollweide projection with a central meridian of 136°E longitude. Black dashed line: dichotomy boundary of Andrews-Hanna et al. (2008), dotted gray line: boundary of the Terra Cimmeria-Sirenum province (Bouley et al., 2020), red star: location of the Gale crater (Cousin et al., 2017), gray star: location of the Khujirt crater (Lagain et al., 2022), red triangles: locations of feldspar-rich outcrops revealed by orbital spectroscopy (Carter & Poulet, 2013; Payré et al., 2022; Phillips et al., 2022; Wray et al., 2013).

(Tharsis and Elysium), where the bulk density may reach $3,000-3,200 \, \mathrm{kg} \, \mathrm{m}^{-3}$ (Goossens et al., 2017). Variations in the Calcium content of pyroxene between Hesperian and Noachian igneous rocks cannot explain such large density differences (Baratoux et al., 2014; Mangold et al., 2010). The presence of a mega-regolith with a high porosity (\sim 10%) over a non-negligible portion of the crust, or of sedimentary rocks made of clays and sulfate (Wieczorek et al., 2022), may partly explain the low density values found in the highlands. But, given their small contribution to the bulk crust, less than 2% in mass (Mclennan, 2012), their effects are probably insufficient. It has thus been proposed that a large felsic component may be buried beneath the surface in the highlands (Baratoux et al., 2014; Sautter et al., 2015).

Orbital observations have identified outcrops rich in silica (Bandfield, 2006; Christensen et al., 2005; Michalski et al., 2024) or in iron-rich feldspar (Figure 1, red triangles, Carter & Poulet, 2013; Payré et al., 2022; Phillips et al., 2022; Wray et al., 2013) in the highlands, that could represent felsic rocks, but their degree of differentiation is still debated (Barthez et al., 2023; Flahaut et al., 2023; Phillips et al., 2022). In parallel, a large diversity of igneous rocks has been detected in the Gale crater, from mafic rocks, typical of the Martian surface, to intermediate and evolved rocks, such as trachytes, dated to the Noachian/late Hesperian (Cousin et al., 2017; Sautter et al., 2015). Pairs of meteorites, like NWA 7034 and NWA 7533, breccia fragments of the same parent meteorite, contain differentiated clasts ranging from intermediate to monazite in composition, mixed with larger basaltic and gabbroic clasts (Agee et al., 2013; Humayun et al., 2013; Santos et al., 2015). The formation of this breccia occurred only 225 Myr ago, but felsic clasts are as old as 4.35–4.49 Gyr (Cassata et al., 2018; Costa et al., 2020), indicating that felsic rocks were present on early Mars. Unlike other Martian meteorites, this breccia appears to be representative of the Martian highlands, because of its high concentration in Fe, K and Th, its strong magnetic signature and the ancient crystallisation ages of its minerals. The crater Khujirt, located in the north-east of the Terra Cimmeria-Sirenum province, in the Southern Hemisphere of Mars, was identified as the possible ejection

BONNET GIBET ET AL. 2 of 31

site (Lagain et al., 2022). In addition, several feldspar-rich outcrops of potentially evolved composition have been detected by visible/near-infrared spectroscopy in this province (Payré et al., 2022), which concentrates evidence for the presence of felsic rocks.

Observations of differentiated rocks are all located in the highlands (Figure 1), which present a high topography and ancient terrains contrasting with the low topography and younger terrains of the north. Assuming a uniform crustal density, the hemispheric difference in topography would be caused by a difference in crustal thickness. But if the highlands contain a buried felsic component, its bulk density could be lower than that of the northern crust, which would explain at least part of the dichotomy in topography (Knapmeyer-Endrun et al., 2021; Wieczorek et al., 2022). With a north-south crustal density contrast of 200–300 kg m⁻³, a prominent dichotomy in crustal thickness would no longer exist. It is therefore important to understand the mechanism behind the formation of these differentiated rocks to constrain the bulk crustal density of these geological provinces and the nature of the dichotomy.

On modern Earth, felsic rocks mostly form in subduction settings; however, there is no evidence of any past plate tectonic activity on Mars. A primary origin for the remotely-detected feldspar-rich rocks has been proposed, in particular because the remote detection of plagioclase is difficult and may require an enrichment of over 90% in anorthite, as in the lunar highlands (Carter & Poulet, 2013; Wieczorek et al., 2022; Wray et al., 2013). But the formation of an anorthosite flotation crust seems more difficult on Mars than on the Moon (Collinet et al., 2015; Elkins-Tanton, 2012; Elkins-Tanton et al., 2003): anorthite crystals are stable at pressures below ~1 GPa, that is, only over the first hundred kilometers on Mars, and the presence of water also reduces the stability of plagioclase (Lin et al., 2017). Alternatively, large Ca-rich plagioclase crystals may be more easily detected by remote-sensing (Barthez et al., 2023), which would require an anorthite concentration of only ~30%–80%. Nyquist et al. (2016) also proposed that the evolved clasts of NWA 7034 formed similarly to lunar KREEP-enriched rocks, that is, by extraction of residual melts enriched in incompatible elements from the crystallizing magma ocean. But, crystallisation experiments have shown that the melt composition remains predominantly basaltic until the end of crystallisation of the Martian mantle (Collinet et al., 2015). Impacts may also bring felsic material to Mars (Payré et al., 2022, 2024), or generate partial melts of evolved composition (Black & Marchi, 2024). However, the rocks found at Gale crater form a magmatic series, that is an alkaline suite issued from a basaltic magma (Sautter et al., 2015), which argues for their secondary origin. Their chemistry and mineralogy are comparable to those of differentiated terrestrial intraplate volcanic rocks (Udry et al., 2018), suggesting they formed by fractional crystallisation, in presence of water, of an ultramafic or mafic melt similar in composition to the Martian crust. Ostwald et al. (2022) demonstrated that the compositions of this alkaline suite rocks are in fact better reproduced when accounting for assimilation of crustal rocks in addition to fractional crystallisation of a primary melt from the Martian mantle.

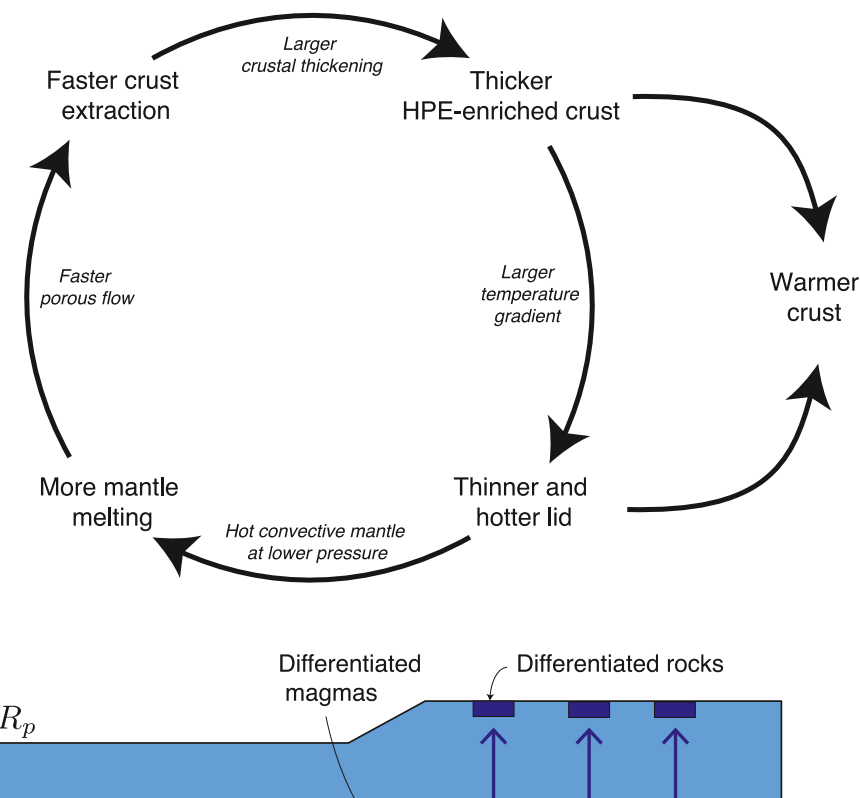
On one-plate planets like Mars, the crustal thickness exerts a positive feedback on mantle melt extraction. As the crust concentrates heat-producing elements, the lithosphere is hotter and thinner in regions of thicker crusts (Plesa et al., 2018; Thiriet et al., 2018). The mantle melt fraction as well as the rates of melt extraction and crust thickening are therefore higher where the crust is thicker. This mechanism enables the formation of geological provinces of thick crust at large wavelengths, in particular at the hemispheric scale, as the effectiveness of conductive cooling is increased at smaller wavelengths; this mechanism can thus explain the Martian dichotomy (Figure 2, Bonnet Gibet et al., 2022). This mechanism further implies that regions of thicker crusts are characterized by an increased magmatism and are marked by higher temperatures. Following what has been proposed for the stabilization of Archean cratons on Earth (Atherton & Petford, 1993; Jaupart et al., 2018; Mareschal & Jaupart, 2006; Sizova et al., 2015), we here investigate whether partial melting can be sustained in the deep crust, in particular in regions of thick crust. In that case, fractional crystallization of new incoming mantle melts together with crustal assimilation would generate more evolved magmas as demonstrated by Ostwald et al. (2022). The resulting buoyant magmas could then ascend toward the surface and form differentiated rocks enriched in silica and alkali, that is, felsic rocks. In this scenario, felsic rocks would form concomitantly to the crust and dichotomy on Mars, and preferentially in regions of thick crusts, as observed (Figures 1 and 2).

To explore this scenario, we use and develop further the asymmetric 1D thermal evolution model described in Bonnet Gibet et al. (2022) to quantify partial melting in the crust over time. We first describe the modifications brought to our physical model and illustrate a specific thermal evolution that shows two episodes of partial melting in the southern crust. To estimate the probability of Martian crust differentiation given our current

BONNET GIBET ET AL. 3 of 31

onlinelibrary.wiley.com/doi/10.1029/2024IE008486 by Dtsch Zentrum F. Luft-U. Raum Fahrt In D. Helmholtz Gemein.

Wiley Online Library on [06/10/2025]. See the Terms



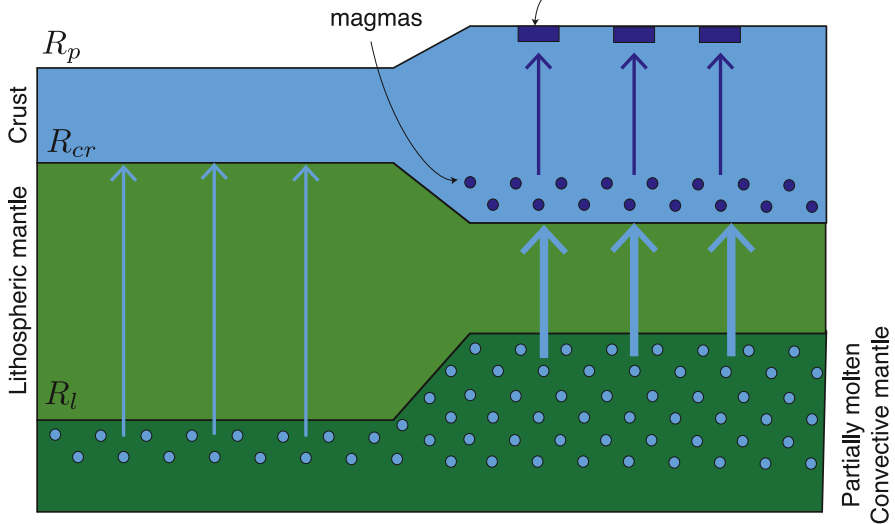


Figure 2. Conceptual diagram showing the positive feedback of the crust thickness on melt extraction. The crust is enriched in heat-producing elements leading to larger lithospheric temperatures where the crust is thicker. The rheological temperature marking the boundary between the convective mantle and the lid is reached at shallower depths, that is, the lid is thinner, below a thicker crust. The well-mixed convective mantle rises to lower pressures and mantle melt fractions are higher below thinner lids because of the pressure-dependence of the solidus. By Darcy's law, the extraction rate is higher where the melt fraction is larger. Therefore, larger thickening rates are expected where the crust is thicker. This mechanism also implies that the base of the crust is hotter, and partial melting more likely, where the crust is thicker. Extraction of evolved partial melts could lead to differentiated rocks at shallower depths.

knowledge on the thermal state of Mars, we use our thermal model in a Bayesian inversion based on the recent constraints on Mars' structure (crustal thickness and mantle thermal state) provided by the NASA InSight mission. This inversion gives a set of thermal evolutions, each defined by an ensemble of parameters, that reproduce the observations from InSight. We study the subset of inverted thermal evolutions that are able to sustain partial melting and differentiation of the crust in the south. We finally discuss the differences between the two sets of evolutions.

BONNET GIBET ET AL. 4 of 31

2. Thermal Evolution Modeling

We use a parameterized convection model, which considers a well-mixed convective mantle topped by a stagnant lid, where the heat is transported by conduction (Breuer & Spohn, 2006; Hauck & Phillips, 2002; Morschhauser et al., 2011). The well-mixed mantle is characterized by a temperature T_m at its top and an isentropic temperature profile (Thiriet et al., 2018). We thus neglect lateral temperature variations that naturally arise in convection flows (J. H. Roberts & Zhong, 2006). We consider, as in Thiriet et al. (2018) and Bonnet Gibet et al. (2022), a lid separated in two different hemispheres with different temperature profiles $T^{\text{N/S}}(r,t)$, lid thicknesses $D_t^{\text{N/S}}$, mantle average melt fractions $\phi_a^{\rm N/S}$, crustal thicknesses $D_{cr}^{\rm N/S}$ and crust enrichments in heat-producing elements compared to bulk silicate Mars $\Lambda_{cr}^{N/S}$, where the subscripts N/S refer to values for the Northern (N) or Southern Hemisphere (S) respectively. We impose an initially small hemispherical perturbation ΔD_i^0 in lid thickness to trigger a differential growth of the lid and crust in between the two hemispheres. Bonnet Gibet et al. (2022) provided a complete description of this model, but its essential ingredients are recalled. To obtain a better resolution of the temperature profile in the lid, the heat source term due to magmatism is better specified. We also consider the cooling caused by downward advection of material in the lid associated to magma eruption and intrusion in the crust, which was previously neglected. Finally, we parameterize a basalt solidus for the crust of Mars and calculate the melt fraction in the crust as a function of depth. We neglect cooling induced by extraction and eruption of differentiated crustal melts that may form.

2.1. Heat Conservation in the Mantle and Core

The convective heat flow $q_{\rm cm}$ that controls both the mantle temperature and the growth of the lid is parameterized from the Rayleigh number $Ra_u = \frac{\alpha \rho_m g_u (T_m - T_l) d^3}{\kappa \eta_u}$ after the boundary layer theory (Turcotte & Schubert, 2002):

$$q_{\rm cm} = k_m \frac{T_m - T_l}{\delta_u} = k_m \frac{T_m - T_l}{d} \left(\frac{Ra_u}{Ra_u^{\rm crit}} \right)^{0.335},\tag{1}$$

where k_m is the thermal conductivity of the mantle, $d = R_p - R_c - D_l$ the convective layer thickness, δ_u the thickness of the top boundary layer, T_l the temperature at the base of the lid (Davaille & Jaupart, 1993; Thiriet et al., 2019) and Ra_u^{crit} the critical Rayleigh number which is constant for the top boundary layer (Table 1). The core-mantle boundary (CMB) heat flow q_c that controls core cooling is similarly parameterized from the Rayleigh number $Ra_c = \frac{\alpha \rho_m g_c (T_b - T_c) d^3}{\kappa \eta_c}$:

$$q_{c} = k_{m} \frac{T_{b} - T_{c}}{\delta_{c}} = k_{m} \frac{T_{b} - T_{c}}{d} \left(\frac{Ra_{c}}{Ra_{c}^{crit}} \right)^{1/3}, \tag{2}$$

where δ_c is the thickness of the bottom boundary layer, T_b is the temperature at the top of this boundary layer, T_c is the CMB temperature and $Ra_c^{\rm crit}$ is the critical Rayleigh number at the base of the mantle which is computed following Deschamps and Sotin (2001). The Rayleigh number depends essentially on the mantle viscosity which follows an Arrhenius law:

$$\eta(T,P) = \eta_0 \exp\left(\frac{A+PV}{RT} - \frac{A+P_0V}{RT_0}\right),\tag{3}$$

where T is temperature, P pressure, η_0 the reference viscosity at the reference temperature $T_0 = 1600$ K and pressure $P_0 = 3$ GPa, R the gas constant, A the activation energy and V the activation volume. Heat conservation in the mantle and core give their thermal evolution:

$$\rho_m c_m V_{cm} \epsilon_m (St+1) \frac{\mathrm{d}T_m}{\mathrm{d}t} = -\sum_{l}^{N/S} (q_{cr}^{N/S} + q_{cm}^{N/S}) A_{cm}^{N/S} + q_c A_c + H_{cm} V_{cm}, \tag{4}$$

$$\rho_c c_c V_c \epsilon_c \frac{\mathrm{d} T_c}{\mathrm{d} t} = -q_c A_c,\tag{5}$$

BONNET GIBET ET AL. 5 of 31

Table 1
Parameters of Our Model

Parameters of	Our Model		
Parameter	Description	Value	Unit
R_p	Planet radius	3,390	km
R_c	Core radius	1,825	km
f	Lowlands area fraction	0.41	
$ ho_c$	Core density	6,200	${\rm kg}~{\rm m}^{-3}$
ρ_p	Primordial mantle density	3,472	${\rm kg}~{\rm m}^{-3}$
$ ho_{cr}$	Crustal density	2,550 to 3,150	${\rm kg}~{\rm m}^{-3}$
k_{cr}	Crustal thermal conductivity	2 to 4	$W\ m^{-1}\ K^{-1}$
k_m	Mantle thermal conductivity	4	$W \ m^{-1} \ K^{-1}$
c_c	Core heat capacity	840	$J K^{-1} kg^{-1}$
c_{cr}	Crust heat capacity	1,000	$J K^{-1} kg^{-1}$
c_m	Mantle heat capacity	1,142	$J K^{-1} kg^{-1}$
α_m	Thermal expansion coefficient	2.5×10^{-5}	K^{-1}
L_m	Latent heat of mantle crystallization	5×10^{5}	$\rm J~kg^{-1}$
L_{cr}	Latent heat of crust crystallization	3×10^{5}	$\rm J~kg^{-1}$
D_i	Partition coefficient	0.01	
$ ho_{ m liq}^0$	Magma density at 0 GPa	2,600	${\rm kg}~{\rm m}^{-3}$
χ	Isothermal compressibility	0.04	GPa^{-1}
f_{mag}	Magmatism fraction	0 to 1	
f_{base}	Basal magmatism fraction	0 to 1	
g_u	Surface gravity	3.7	$\mathrm{m}\ \mathrm{s}^{-2}$
g_c	Core-Mantle boundary gravity	3.4	$\mathrm{m}\ \mathrm{s}^{-2}$
ϵ_c	Ratio of the mean to upper core temperature	1.1	
P_0	Reference pressure	3	GPa
T_0	Reference temperature	1,600	K
A	Activation energy	250 to 400	kJ mol ⁻¹
a_{rh}	Rheological coefficient	2.54	
R	Gas constant	8.314462	$\rm J~mol^{-1}~K^{-1}$
η_0	Reference viscosity	10^{19} to 10^{22}	Pa s
V	Activation volume	0 to 8	cm^3
β_u	Upper boundary layer exponent	0.335	
β_c	Lower boundary layer exponent	1/3	
Ra_u^{crit}	Upper critical Rayleigh number	450	
k_0	Mantle reference permeability		m^2
η_l	Melt viscosity		Pa s
ζ	Reference permeability to melt viscosity ratio (PtV ratio)	10^{-12} to 10^{-7}	$m^2 \ Pa^{-1} \ s^{-1}$
ϕ_c	Critical melt fraction	0.02	
D_{ref}	Crust thickness corresponding to 20% of silicate volume	191	km
ΔT_{sol}	Increase in solidus for a crust thickness Dref	150	K
$X_{\mathrm{H}_2\mathrm{O}}^p$	Primordial mantle water content	0.00 to 0.05	%wt H ₂ O
D_l^0	Initial lid thickness	20 to 200	km
D_{cr}^0	Initial crust thickness	4	km
T_s	Surface Temperature	220	K
T_m^0	Initial upper mantle temperature	1,625 to 1,750	K

BONNET GIBET ET AL. 6 of 31

Table 1 Continued			
Parameter	Description	Value	Unit
ΔT_c^0	Initial superheating of the core	150	K
Λ_{cr}^0	Initial enrichment of the crust	10	
ΔD_l^0	Initial N-S difference in lid thickness	0.5 to 12	km

where ρ_m is the mantle density, c_m the mantle heat capacity, V_{cm} the volume of the convective mantle, $St = \frac{L_m V_\phi}{c_m V_{cm}} \frac{\mathrm{d}\phi_a}{\mathrm{d}T_m}$ the time-dependent Stefan number in which V_ϕ is the partially molten volume of the mantle, ε_m the ratio between the average temperature of the convective mantle and the temperature at the top, $q_{cr}^{\mathrm{N/S}}$ the heat flux caused by melt extraction, A_c the surface of the CMB, H_{cm} the mantle internal heating, V_c the core volume, ρ_c the core density, c_c the core heat capacity and e_c the average core temperature to CMB temperature ratio.

Initially, a temperature at the top of the convective mantle T_m^0 , a lid thickness D_l^0 and a super-heating of the core ΔT_c^0 , due to core formation and associated dissipation of gravitational potential energy (Breuer & Spohn, 2003), are prescribed (see Section 4.2). The initial CMB temperature is thus given by $T_c^0 = T_m^0 + \frac{\alpha g T_m^0}{c_m} (R_l^0 - R_c) + \Delta T_c^0$.

The lid thickness evolution is determined from a heat balance at the interface between the lid and the convective mantle:

$$\rho_m \left(c_m (T_m - T_l) + L_m \phi_a^{\text{N/S}} \right) \left(\frac{\mathrm{d}D_l^{\text{N/S}}}{\mathrm{d}t} - w^{\text{N/S}} \right) = -q_{cm}^{\text{N/S}} - k_m \frac{\partial T}{\partial r} \Big|_{r=R_l}^{\text{N/S}}, \tag{6}$$

where L_m is the latent heat of crystallisation, w the melt extraction rate and $\frac{\partial T}{\partial r}\Big|_{r=R_l}^{N/S}$ the temperature gradient at the base of the lid

The rate of crustal extraction depends on the melt percolation rate in the partially molten layer of the convective mantle and may differ in between both hemispheres (McKenzie, 1985; Richter & McKenzie, 1984):

$$\frac{\mathrm{d}D_{cr}^{\mathrm{N/S}}}{\mathrm{d}t} = w^{\mathrm{N/S}} \left(\frac{R_l^{\mathrm{N/S}}}{R_{cr}^{\mathrm{N/S}}}\right)^2 = \left[\frac{k_0 \phi_{\mathrm{eff}}^3 \Delta \rho g_u}{\eta_1} (1 - \phi_{\mathrm{eff}}) \left(\frac{R_l}{R_{cr}}\right)^2\right]^{\mathrm{N/S}},\tag{7}$$

where k_0 is a reference permeability for the host rocks (Miller et al., 2014), $\phi_{\rm eff}$ the effective average melt fraction of the partially molten zone (Bonnet Gibet et al., 2022), η_1 the melt viscosity (Giordano et al., 2008), $\Delta \rho = \rho_m - \rho_0^{\rm liq}(1 + \chi P)$ the melt-host rock density difference accounting for melt compressibility χ . Since both the reference permeability and the melt viscosity can span several orders of magnitude and are poorly constrained, we explore variations in their ratio $\zeta = k_0/\eta_1$, noted PtV ratio.

The enrichment in heat-producing elements and water of the liquid forming the crust is obtained by considering a chemical equilibrium and the same partition coefficient D_i for all heat-producing elements and water. Conservation of the amount of radioelements and water give the evolution of their concentrations in the crust and mantle (Bonnet Gibet et al., 2022). Contrary to Fraeman and Korenaga (2010) or Plesa and Breuer (2014), we do not consider that the residue left after crustal extraction forms a rigid layer that thickens the lid and limits further mantle melting, but that it mixes with the rest of the mantle, leading to a homogeneous concentration of HPEs and water in the convective mantle.

2.2. Heat Conservation in the Lid

In each hemisphere, we solve for the diffusion equation in spherical geometry over the lid thickness accounting for heat brought by magmatism H^{mag} , downward advection of heat with lithospheric material at velocity u(r) caused by crust growth as well as crustal melting:

BONNET GIBET ET AL. 7 of 31

Table 2
Outputs of Our Model

Parameter	Description	Computation	Unit
$D_{cr}^{ m N/S}$	Crust thickness	4th order Runge-Kutta integration of Equation 7	km
$D_l^{ m N/S}$	Lid thickness	4th order Runge-Kutta integration of Equation 6	km
T_p	Mantle potential temperature	Equation 29	K
T_c	CMB temperature	4th order Runge-Kutta integration of Equation 5	K
$D_{cr}^{ m avg}$	Average crustal thickness	$R_p - \left(fR_{cr}^{N^3} + (1-f)R_{cr}^{S^3}\right)^{1/3}$	km
$\Lambda_{cr}^{ m N/S}$	Crust enrichment	Mass balance, see Bonnet Gibet et al. (2022)	
$F_{ m HPE}^{cr}$	Percentage of internal heating in the crust	$\frac{\rho_{cr}\left(f\Lambda_{cr}^{N}\left(Rp^{3}-R_{cr}^{N^{3}}\right)+(1-f)\Lambda_{cr}^{S}\left(R_{p}^{3}-R_{cr}^{S^{3}}\right)\right)}{\rho_{p}\left(R_{0}^{3}-R_{c}^{2}\right)}$ × 100	%
$\Phi(r)$	Mantle melt fraction profile	non-linear evolution with T, see Bonnet Gibet et al. (2022)	
V_{ϕ}	Mantle molten volume	$\int dV$ where $\Phi(r) > 0$	m^3
ϕ_a	Average mantle melt fraction	$rac{1}{V_\phi} \int_{V_\phi} \Phi(r) dV$	
$\phi_{ m eff}$	Effective mantle melt fraction	$\int_{V_{\phi}} \max \left[\left(\Phi(r) - \phi_c \right), 0 \right] dV$	
$V_{\phi_{cr}}$	Crustal volume with partial melt	$\int dV$ where $\phi_{cr}(r) > 0$	m^3
$\phi_{cr}^{ m avg}$	Average crustal melt fraction	$rac{1}{V_{\phi_{cr}}} \! \! \int_{V_{\phi_{cr}}} \! \! \phi_{cr}(r) dV$	

$$\rho(r)c(r)\left[\left(1+a(r)\frac{L(r)}{c(r)\Delta T^{\text{ls}}(r)}\right)\frac{\partial T}{\partial t}+u(r)\left(\frac{\partial T}{\partial r}+\frac{L(r)}{c(r)}\frac{\partial \phi}{\partial r}\right)\right]=\frac{1}{r^2}\frac{\partial}{\partial r}\left(r^2k(r)\frac{\partial T}{\partial r}\right)+H^{\text{rad}}(r,t)+H^{\text{mag}}(r,T,t),$$
(8)

where k(r) is the thermal conductivity, equal to $k_{\rm cr}$ in the crust and k_m in the mantle, c(r) is the heat capacity, equal to c_m in the mantle and c_{cr} in the crust, L(r) is the latent heat of melting equal to L_m in the mantle and L_{cr} in the crust and $\rho(r)$ is the density, equal to ρ_{cr} in the crust and ρ_m in the mantle. Magmatism induces a heating term noted $H^{\rm mag}(r,T,t)$ that depends on crustal temperatures and the fraction of basal and bulk intrusive magmatism (see Section 2.3.1); it is set to zero in the lithospheric mantle. Downward advection of colder material and hence heat occurs at velocity u(r), which depends on the crustal growth rate (see Section 2.3.2) and on the temperature and melt fraction gradients. We neglect changes in the thermodynamic parameters of the crust caused by melting, as melt fractions in the crust remain low. Crustal melting is added as a heat source/sink term, function of the secular cooling term, the Stefan number for the crust $St(r) = L(r)/(c(r)\Delta T^{\rm ls}(r))$, and a parameter a(r), where a(r) = 1 if the melt fraction $\phi(r)$ is larger than 0 and a(r) = 0 if $\phi(r) = 0$ or 1. $\Delta T^{\rm ls}(r) = T_{\rm liq}(r) - T_{\rm sol}(r)$ is the difference between the liquidus and solidus of the crust (See Section 2.4, Equations 13 and 19).

2.3. Magma Emplacement

2.3.1. Magma Heating

We neglect heat loss during magma ascent through the lid and assume that magma intrudes the crust at the temperature of the lid base T_l . The heat source term caused by magma cooling in the crust depends on how the magma is distributed within the crust. We consider that a fraction of magma f_{mag} intrudes the crust while a fraction $1 - f_{\text{mag}}$ erupts at the surface. The intrusive fraction is itself divided into a basal component noted as "basal magmatism" f_{base} , deposited at the crust base, while the fraction $1 - f_{\text{base}}$ distributes uniformly in the crust as "crustal intrusions." We consider that the heat released by volcanism at the surface is instantaneously evacuated. The heat source term caused by magmatism depends thus on the crustal temperature and radius and writes:

$$H^{\text{mag}}(r > R_{cr}) = w \frac{A_{cm}}{V_{cr}^{\text{N/S}}} \rho_{cr} \left[L_{cr} \left(1 - \phi_{cr}(r) \right) + c_{cr} (T_l - T(r)) \right] f_{\text{mag}} \left(1 - f_{\text{base}} \right), \tag{9}$$

$$H^{\text{mag}}(R_{cr}) = w A_{cm} \rho_{cr} \left[L_{cr} \left(1 - \phi_{cr}(R_{cr}) \right) + c_{cr}(T_l - T_{cr}) \right] f_{\text{mag}} \left(\frac{\left(1 - f_{\text{base}} \right)}{V_{cr}^{\text{N/S}}} + \frac{f_{\text{base}}}{dV_{cr}} \right), \tag{10}$$

BONNET GIBET ET AL. 8 of 31

where the crust-mantle boundary is at radius R_{cr} and temperature T_{cr} , w is the melt percolation velocity at the interface between the lid and mantle, of radius R_l , and area A_{cm} . $V_{cr}^{N/S}$ is the crust volume corresponding to the crustal thickness $D_{cr}^{N/S}$ and dV_{cr} is the volume element heated by basal magmatism which in our model corresponds to the elemental numerical volume at the base of the crust.

2.3.2. Downward Advection of Heat Due To Crustal Growth

Magma intrusion and crustal thickening lead to the downward displacement of underlying crustal and lid materials. This acts to cool down the lid as it brings colder material downward, which limits heating by magmatism. This effect is generally neglected in parameterized thermal evolution studies (Breuer & Spohn, 2006; Morschhauser et al., 2011), in particular because the Péclet number $\left(\frac{\rho c D_i w}{k}\right)$ is less than one (Foley & Smye, 2018). In the new version of our model, we account for this effect, as it can limit the rise in crustal temperatures associated to magmatism.

The distribution of magma intrusions and extrusions determines the downward advection: extrusive volcanism causes downward displacement of the entire crust and lid, while basal magmatism leads to the downward advection of the lithospheric mantle only. The downward displacement velocity u(r) in the crust $(r > R_{cr})$ and in the lithospheric mantle $(R_1 \le r \le R_{cr})$ due to volcanism and magmatism is obtained by volume conservation:

$$u(r > R_{cr}) = -\left(1 - f_{\text{mag}}\right) \times w \left(\frac{R_l}{r}\right)^2 - \left(1 - f_{\text{base}}\right) \times f_{\text{mag}} \times w \frac{R_l^2}{r^2} \frac{R_p^3 - r^3}{R_p^3 - R_{cr}^3},\tag{11}$$

$$u(r \le R_{cr}) = -w \times \left(\frac{R_l}{r}\right)^2,\tag{12}$$

where R_n is the radius of Mars.

2.4. Partial Melting of the Crust

A characteristic solidus for the Martian crust has not yet been proposed. We thus rely on existing experiments on terrestrial basaltic analogs to propose an approximate solidus for Mars that depends on pressure and water content, as the solidus of mafic rocks is strongly modified by addition of water. For the Earth, the solidus of rocks with basaltic compositions has been determined for subduction settings where rocks are often altered and/or enriched in water (Green & Ringwood, 1967; Peacock et al., 1994; Sisson & Kelemen, 2018). The water composition of the Martian primordial mantle is estimated between 1 and 1000 ppm (Johnson et al., 1991; Mysen et al., 1998) which is not sufficient to significantly affect the melting temperature of the Martian mantle. Still, as water and heatproducing elements share similar partition coefficients (Aubaud et al., 2004), the crust of Mars may be similarly enriched in water and heat-producing elements, that is, 10 to 15 times more enriched than the primitive mantle (Thiriet et al., 2018). Considering the highest possible enrichment of 1.5 wt % water for the Martian crust, it still seems much lower than for a terrestrial basalt (~2%-5% Green & Ringwood, 1967; Peacock et al., 1994; Sisson & Kelemen, 2018) but appears close to that of a water-enriched terrestrial mantle (Katz et al., 2003). We parameterize the depression of the crustal solidus resulting from the presence of water similarly to Katz et al. (2003), assuming that basalts would behave like mantle rocks as they have a similar mineralogical assembly. We use a function of the melt fraction water content $X_{H,O}$ and pressure P, in GPa, with a classical slope of 100 K GPa⁻¹:

$$T_{\text{sol}}^{\text{cr}}(P, X_{H_2O}) = T_{\text{sol}}^{\text{cr},0} + 100P - \Delta T(X_{H_2O}),$$
 (13)

where $T_{\rm sol}^{\rm cr,0}$ is in Kelvin. $T_{\rm sol}^{\rm cr,0}$ is the Martian crustal solidus temperature in K at zero pressure, defined as $T_{\rm sol}^{\rm cr,0} = T_{\rm sol}^{\rm Earth,0} - \Delta T_{\rm Fe}$, where $T_{\rm sol}^{\rm Earth,0}$ is the typical solidus temperature at zero pressure for a terrestrial basalt (1,323 K, Peacock et al., 1994) and $\Delta T_{\rm Fe}$ is a correction accounting for different #Mg between the bulk silicate part of the Earth and that of Mars. We use a temperature difference of 50 K as estimated by Collinet et al. (2015) for the difference in solidus between the Martian and Earth's mantles. $\Delta T(X_{H_2O})$ is the decrease in solidus temperature caused by addition of water in the melt, expressed as a power law, function of the melt water content in wt%:

BONNET GIBET ET AL. 9 of 31

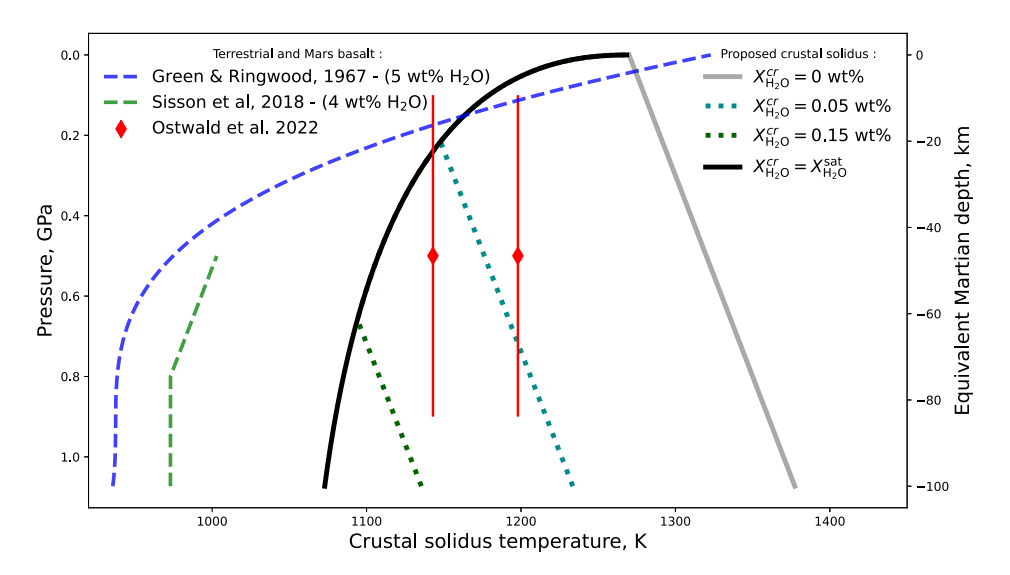


Figure 3. Crustal solidus temperature $T_{\rm sol}^{\rm cr}$ as a function of pressure (in GPa) and equivalent Martian depth (in km) assuming a crustal density of 2900 kg m⁻³ and a gravity of 3.7 m²s⁻¹. The solid and dotted curves represent the Martian crustal solidus for increasing values of water content in the crust $X_{\rm H_2O}^{\rm cr}$ from 0 to 1,500 ppm with 500 ppm increments. The black solidus curve is the solidus at water saturation ($X_{\rm H_2O} = X_{\rm H_2O}^{\rm sat}$). The gray solid curve is the anhydrous solidus. Different water-saturated solidus for terrestrial basalts are plotted for comparison in dashed lines as a function of pressure. The red diamonds represent two solidus temperatures for the crust calculated by Ostwald et al. (2022) for two different compositions using Rhyolite-MELT and the error bars represent the pressure range used in their models.

$$\Delta T(X_{\rm H,O}) = KX_{\rm H,O}^{\gamma},\tag{14}$$

where we use K = 43 K wt%⁻⁷ and $\gamma = 0.75$ as in Katz et al. (2003) for the terrestrial mantle solidus. The water content in the melt at the solidus ($\phi_{cr} = 0$) is obtained assuming chemical equilibrium:

$$X_{\rm H_2O} = \frac{\Lambda_{cr} X_{\rm H_2O}^p}{D_i},\tag{15}$$

with $X_{H_2O}^p$ the primitive mantle water content, Λ_{cr} the water enrichment of the crust relative to the primitive mantle. This enrichment factor is the same as for heat producing elements as we assume the same partition coefficient D_i for all these elements (Aubaud et al., 2004). The decrease in solidus temperature associated to the addition of dissolved water in the melt is limited by water saturation:

$$\Delta T(X_{\text{H}_2\text{O}} > X_{H_2\text{O}}^{\text{sat}}) = \Delta T(X_{\text{H}_2\text{O}}^{\text{sat}}),\tag{16}$$

where $X_{H_2O}^{\text{sat}}$ is the maximum water content in the melt, which depends on pressure following:

$$X_{\rm H_2O}^{\rm sat} = 12P^{0.6} + P,\tag{17}$$

where P is expressed in GPa and $X_{\rm H_2O}^{\rm sat}$ is in wt% (Katz et al., 2003). A water content similar to that of the primitive mantle as proposed by G. J. Taylor (2013) (i.e., 300 \pm 150 ppm) is sufficient to significantly decrease the crustal solidus temperature compared to the anhydrous one (Figure 3).

The crustal melt fraction is then assumed to be a linear function of temperature over the melting interval:

$$\phi_{cr}(r) = \frac{T(r) - T_{\text{sol}}^{\text{cr}}(r)}{T_{\text{liq}}^{\text{cr}}(r) - T_{\text{sol}}^{\text{cr}}(r)},$$
(18)

BONNET GIBET ET AL. 10 of 31

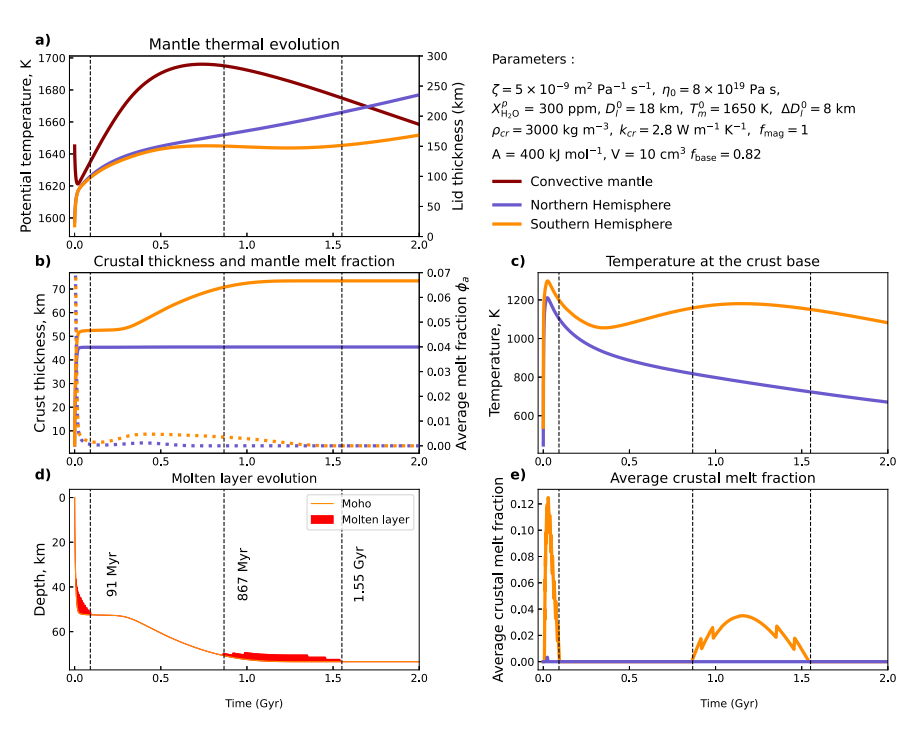


Figure 4. An example of thermal evolution featuring crustal melting. Blue lines are for the north, orange lines are for the south. Evolution of (a) north and south lid thicknesses $D_{\rm l}$, (right y-axis) and potential mantle temperature T_p (solid brown line, left y-axis), (b) north and south crustal thicknesses $D_{\rm cr}$ (solid lines, left axis) and average mantle melt fractions ϕ_a (dotted lines, right axis) (c) temperatures at the base of the crust in the north and south, (d) thickness and depth of the molten layer (in red) in the crust in the south and (e) north and south average crustal melt fractions $\phi_{cr}^{\rm avg}$. We define the average crustal melt fraction as the volumetric average of the melt fraction over the partially molten crustal volume (Table 2). Dotted black lines indicate the different stages of crustal melting.

where $T_{\text{liq}}^{\text{cr}}(r)$ is the crustal liquidus in Kelvins, equal to the anhydrous solidus plus a constant:

$$T_{\text{liq}}^{\text{cr}}(P) = T_{\text{sol}}^{\text{cr},0} + 100P + 330.$$
 (19)

With this parameterization, we establish a saturation solidus (Figure 3, black curve) where the melt water content consistently equals saturation, maximizing the impact of water. At zero pressure, this solidus is similar to the anhydrous case; it progresses to lower temperatures for increasing pressures and depths. Our saturated solidus behavior aligns with that proposed by Green and Ringwood (1967) or Sisson and Kelemen (2018) for terrestrial basalts in subduction zones (dashed curves on Figure 3), although terrestrial basalts show a steeper slope caused by a higher water content. If the melt becomes undersaturated at some depth, the crustal solidus slope transitions to the anhydrous slope (Figure 3, dotted colored curves). The solidus curves are similar to those described in Peacock et al. (1994). Ostwald et al. (2022) calculated two solidus temperatures using Rhyolite-MELTS for two different Martian crust compositions with a water content of 0.14 wt% at unspecified pressures. These temperatures are 1,148 and 1,193 K and fall well in the range of our inferred crustal solidus temperatures (Figure 3, red diamonds).

3. An Example of Thermal Evolution With Crustal Melting

Our model is numerically solved to determine the thermal evolution of Mars and the extraction of the crust over 4.5 Gyr from a given initial state (see Bonnet Gibet et al., 2022, for details on the numerical resolution). The example shown in Figure 4 illustrates a classical thermal evolution for commonly used parameters (Table 1); it features two typical episodes of partial melting in the crust. As shown in Bonnet Gibet et al. (2022), two stages of crustal extraction can occur: an early and a late one (Figure 4b). An episode of crustal melting may occur toward the end of each crustal extraction stage if those stages are important and rapid enough (Figures 4d and 4e).

BONNET GIBET ET AL.

During the first phase of crustal extraction, a thick crust rapidly forms in both hemispheres, within a timescale typically less than ~100 Myr (~40 Myr for the example of Figure 4). The early rapid thickening of the crust is caused by the initially large mantle melt fraction (~18% at 0 Gyr). Temperatures at the base of the crust then rise rapidly and can reach the solidus in the south, as in this example (Figures 4c and 4d), where crustal melting occurs between 6 and 91 Myr (Figures 4d and 4e). As the mantle cools and its melt fraction decreases, it becomes smaller than the critical value for melt extraction, which impedes crustal thickening during ~200 Myr (Figure 4b). The crustal temperature decreases below the crustal solidus (Figures 4c–4e). Meanwhile, the convective mantle temperature increases because of radiogenic heating, while the lid slowly thickens in the north and stabilizes around 150 km in the south (Figure 4a). As a result, the mantle melt fraction increases, and crustal extraction can start again, but only in the south, where the lid is thinner and the melt fraction higher (Figure 4b). During this second phase of crustal thickening in the south, the temperature at the base of the crust starts to rise again at ~300 Myr (Figure 4b) and exceeds the solidus after ~867 Myr (Figure 4e). This second crustal melting event in the south occurs at the end of crust formation for more than 500 Myrs (Figures 4d and 4e).

During the first episode of crustal melting, the average crustal melt fraction reaches 12% in the south over a maximum vertical extent of 8 km but partial melting lasts only for a short duration (<90 Myr). During the second episode, the amplitude of the melting is less important, as the average crustal melt fraction reaches 4% over 3 km, but the episode lasts much longer, ~688 Myr in this case (Figures 4d and 4e). The base of the crust remains partially molten until ~1.55 Gyr, more than 300 Myr after the end of crust formation (Figures 4d and 4e). After this last phase of extraction, the thickness of the crust remains constant (Figure 4b), the temperature of the convective mantle decreases and the stagnant lid thickens (Figure 4a) which impedes further crustal melting.

4. Inversion With a Monte Carlo Markov Chain Algorithm

Our thermal evolution example shows that it is possible to reach the conditions for partial melting at the base of the southern crust during crustal extraction for a given set of parameters. However, this direct approach does not tell us how likely such an episode is. To infer its significance, we first need to define a set of thermal evolution scenarios that are plausible given our current knowledge on the structure and thermal state of Mars. To that aim, an inverse problem is formulated in a Bayesian framework, to estimate the probability of different thermal evolution scenarios, given observations and results of the NASA InSight mission. The inversion is based on a Markov Chain Monte Carlo sampling algorithm, which, through a random walk in our parameter space, defines a collection of models (each model being defined by a set of parameters) that approximates the probability function of our model parameters given the observational constraints.

4.1. Formulation of the Bayesian Inverse Problem

A Bayesian inference is used to formulate our inverse problem following the formalism proposed by Gallagher et al. (2009) and based on Bayes' equation (Bayes, 1763):

$$p(\mathbf{m}|\mathbf{d}) \propto p(\mathbf{d}|\mathbf{m}) \ p(\mathbf{m}),$$
 (20)

where \mathbf{m} represents the parameters of our thermal evolution model and \mathbf{d} represents our "data," which consist of observational constraints on the structure and thermal state of Mars from the InSight mission. $p(\mathbf{m})$ is the prior probability of these parameters and therefore of the associated thermal evolution model. $p(\mathbf{d}|\mathbf{m})$ is the likelihood of our observational data, that is, the probability of \mathbf{d} conditional on our model parameters. $p(\mathbf{m}|\mathbf{d})$ is the posterior probability of the model parameters which we want to reconstruct.

4.2. Prior Distribution

The prior probability $p(\mathbf{m})$ summarizes what we know about our model parameters. Here, we invert 11 parameters, listed in Table 3; the other parameters, held constant, are listed in Table 1. Since we have no specific prior information on these inverted parameters, except for a possible range of values, a uniform probability law is assumed. Thus, the prior probability is 1 for a model whose set of parameters lies within the space defined in Table 3; its prior probability is 0 if it lies outside this space. In addition, we set to 0 the prior probability of models that encounter the situation where the crust becomes as thick as the lithosphere, as it is not entirely clear whether the buoyancy of the crust allows its survival and further growth despite thermal convection (Batra & Foley, 2021;

BONNET GIBET ET AL. 12 of 31

Table 3

Parameters of Our Sampling Algorithm With, ζ the Reference Permeability to Melt Viscosity Ratio, η_0 the Reference Viscosity, f_{mag} the Intrusive Fraction, f_{base} the Fraction of Basal Magmatism, A the Activation Energy, V the Activation Volume, ρ_{cr} the Crust Density, k_{cr} the Crust Thermal Conductivity, X_{H_2O} the Water Concentration of the Primitive Mantle, T_m^0 the Initial Mantle Temperature, ΔD_l^0 the Initial Hemispheric Perturbation in Lid Thickness

Parameters	Minimum	Maximum	$\sigma_{ m perturb}$	Unit
$\log_{10}\zeta$	-12	- 7	0.25	log ₁₀ m ² Pa ⁻¹ s ⁻¹
$\log_{10}\eta_0$	19	22	0.13	log ₁₀ Pa s
$f_{ m mag}$	0	1	0.03	
$f_{\rm base}$	0	1	0.03	
A	250	400	6	kJ mol ⁻¹
V	0	10	0.3	cm ³
$ ho_{ m cr}$	2,550	3,150	30	${\rm kg}~{\rm m}^{-3}$
$k_{\rm cr}$	2.0	4.0	0.06	$W m^{-1}.K^{-1}$
$X_{ m H_2O}^p$	0.0	0.05	0.005	%wt H ₂ O
T_m^0	1,625	1,750	6	K
$\Delta { m D}_l^0$	0.5	12	0.4	km

Bonnet Gibet et al., 2022). Furthermore, these scenarios differ significantly from the solutions we are looking for, as they result in too-thick crusts and/or excessively large dichotomies (Bonnet Gibet et al., 2022); in addition they require very long calculation times.

4.3. Likelihood Function

A thermal evolution scenario generates outputs, obtained during or at the end of the evolution. Some of these outputs can be compared to observations on Mars, thus providing predictions; they are called forecasts. We use four different observational constraints from InSight, described in Section 4.4, which consist of the "data." The data vector \mathbf{d} is composed of the crustal thickness below InSight $D_{\rm InS}^{\rm calc}$, the amplitude of the dichotomy in crustal thickness $\Delta D_{\rm cr}^{\rm calc}$, the mantle potential temperature $T_p^{\rm calc}$ and the average thickness of the thermal lithosphere $D_L^{\rm calc}$. To evaluate the likelihood of the data, we use a Gaussian probability distribution in its general form (Gallagher et al., 2009):

$$p(\mathbf{d}|\mathbf{m}) = \frac{1}{(2\pi)^{N/2} |\mathbf{V}|^{N/2}} \exp\left\{-\frac{1}{2} \left((\mathbf{d} - g(\mathbf{m})^t |\mathbf{V}|^{-1} (\mathbf{d} - g(\mathbf{m})) \right)\right\}, \tag{21}$$

where N=4 is the number of observations, $g(\mathbf{m})$ is the vector containing the model forecasts and \mathbf{V} is the covariance matrix of data errors, which describes

the statistics of both prediction errors and errors in our observational constraints. The covariance matrix is a square of size N^2 composed of the error covariances of each pair of observations. In our case, the observations have no covariance, so the matrix is diagonal and made up of the error variances associated to each observation. In the case of a diagonal covariance matrix, Equation 21 can be written as the product of four probabilities following a Gaussian distribution:

$$p(\mathbf{d}|\mathbf{m}) = p(\Delta D_{cr}|\mathbf{m}) \times p(D_{InS}|\mathbf{m}) \times p(T_{p}|\mathbf{m}) \times p(D_{L}|\mathbf{m}). \tag{22}$$

The probability of $p(X|\mathbf{m})$ follows then a Gaussian law:

$$p(X|\mathbf{m}) = \frac{1}{\sigma_X \sqrt{2\pi}} \exp\left\{-\frac{1}{2} \left(\frac{\bar{X} - X(\mathbf{m})}{\sigma_X}\right)^2\right\},\tag{23}$$

with σ_X the standard deviation of the data and \bar{X} the mean value of the data.

4.4. Observational Data

Observations from the InSight mission have better constrained the structure of the Martian crust and the present-day mantle thermal state. Here, we describe our observational data, their mean values and standard deviations.

4.4.1. Crustal Thickness and Dichotomy Amplitude

The present-day average thickness of the crust and amplitude of the dichotomy are two important forecasts, that is, model outputs that can be compared to observations from InSight.

Data set: Crustal thickness maps can be constructed by joint analysis of the gravity and topography (Knapmeyer-Endrun et al., 2021; Wieczorek et al., 2022). Relative variations of the crustal thickness are obtained by assuming that the Bouguer anomaly comes from undulations of the crust-mantle interface (Wieczorek, 2015). The crust thickness at a given location, estimated from an independent method, then serves as an anchor point to obtain absolute crustal thickness maps. Martian crustal thickness maps have been anchored at the InSight location, where the local crustal thickness has been estimated from receiver function analysis (Durán et al., 2022; Joshi et al., 2023; Knapmeyer-Endrun et al., 2021). The crustal density ρ_{cr} is considered laterally uniform, no north/

BONNET GIBET ET AL. 13 of 31

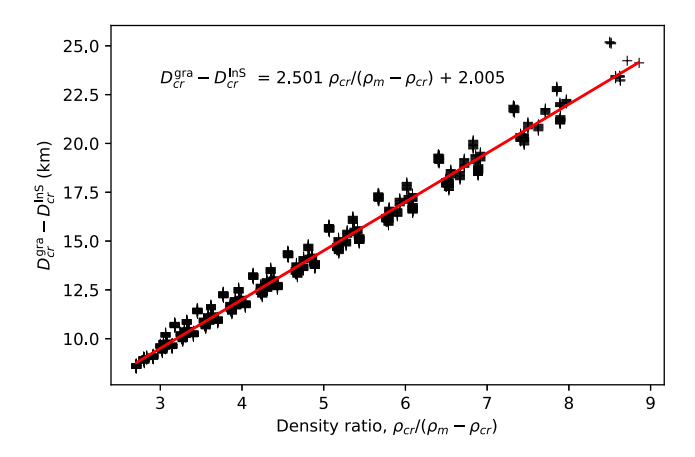


Figure 5. Difference between the global average crustal thickness calculated from Bouguer anomaly inversions and the assumed local crustal thickness at the InSight location as a function of the density ratio between the crustal density and the mantle-crust density contrast for a variety of crustal thickness maps obtained by inversion of gravity and topography data. A linear regression on all data points give the red line whose expression is shown in the graph.

south difference in density is assumed. While partial melting of the crust may occur in one hemisphere and not the other, the bulk density of the crust does not change and remain uniform, even if differentiated melts extract and form a felsic layer, as the residue is then denser than the starting material and the loss of dense mafic crustal residues, as proposed for the continental crust, is not considered here (Jaupart et al., 2018).

We use the results of Wieczorek et al. (2022) which consist of 1833 crustal thickness models built from different combinations of three parameters: the crustal density ρ_{cr} , varying between 2,550 and 3,150 kg m⁻³, the mantle density ρ_m , that is between 3,350 and 3,500 kg m⁻³ and corresponds to different types of mineralogy and the crustal thickness below InSight, estimated between 38 and 48 km. From each modeled crustal thickness map, we extract the global average thickness of the crust $D_{cr}^{\rm gra}$ and the difference in average thickness between the lowlands and the highlands $\Delta D_{cr}^{\rm gra}$, where we use the dichotomy boundary proposed by Andrews-Hanna et al. (2008).

Average crustal thickness: The difference between the average crustal thickness D_{cr}^{gra} extracted from a crustal thickness map and the crustal thickness below InSight D_{InS}^{gra} is linearly correlated to the ratio between the crustal density and the mantle-crust density contrast $\frac{\rho_{cr}}{\rho_m - \rho_{cr}}$ (Figure 5). A linear regression on all data points gives:

$$D_{cr}^{\text{gra}} - D_{\text{InS}}^{\text{gra}} = a_{\text{thick}} \left(\frac{\rho_{cr}}{\rho_{rr} - \rho_{cr}} \right) + b_{\text{thick}}, \tag{24}$$

with a slope $a_{\text{thick}} = 2.501$ km and a y-intercept $b_{\text{thick}} = 2.005$ km; the correlation coefficient (r^2) , equal to 0.998, confirms the strong linear correlation (Figure 5).

The crustal density is a parameter of the thermal evolution model and the mantle density is an output as it increases very slightly with time (from 3,493 to at most 3,500 kg m⁻³) by mass conservation, as the crust is extracted (Bonnet Gibet et al., 2022). Equation 24 is used to predict a theoretical crustal thickness below InSight $D_{\rm InS}^{\rm calc}$ from the outputs and parameters (final average crustal thickness and density ratio) of a given thermal evolution model, to be compared with observations from InSight:

$$D_{\rm InS}^{\rm calc} = D_{\rm cr}^{\rm calc} - a_{\rm thick} \left(\frac{\rho_{cr}}{\rho_m - \rho_{cr}} \right) - b_{\rm thick}. \tag{25}$$

The local crustal thickness below the InSight lander has indeed been estimated using receiver function analysis applied to P and S waves. The most recent works of Durán et al. (2022) and Joshi et al. (2023) give the following estimate:

$$D_{\text{InS}}^{\text{SEIS}} = 43 \pm 5 \text{ km}.$$
 (26)

BONNET GIBET ET AL. 14 of 31

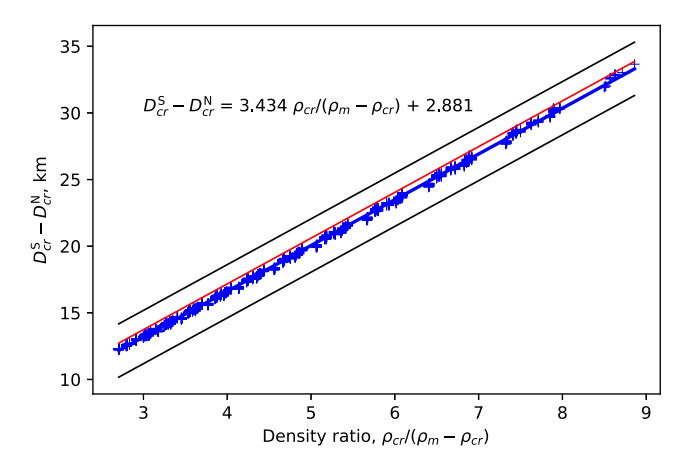


Figure 6. North-south difference in crustal thickness calculated from Bouguer anomaly inversions as a function of the ratio between the crustal density and the density contrast between mantle and crust, where we consider the north-south boundary of Andrews-Hanna et al. (2008). The blue line corresponds to a linear regression on all data points, its expression is shown on the graph. The black lines correspond to a deviation of 2 km from this linear fit. The red curve shows the difference in crustal thickness assuming Airy isostasy and a Highland topography of h = 3.434 km.

The mantle density in our thermal evolution model is an average over the whole mantle volume, but in Bouguer anomaly inversions, it corresponds to the mantle density at the crust-mantle interface. The difference between the density at the top of the mantle and the average mantle density depends on the mineralogical model and ranges between 50 and 200 kg m $^{-3}$. For simplicity, the density at the top of the mantle is considered to be the average mantle density minus 100 kg m $^{-3}$.

Dichotomy amplitude: The difference in north-south crustal thickness obtained from Bouguer anomaly inversions is plotted for each inversion as a function of the same density ratio (Figure 6). We recall that a uniform crustal density is assumed for the crust. A linear regression between the dichotomy amplitude and the density ratio shows a very strong linear correlation with a correlation coefficient of $r^2 = 0.999$. We thus express the expected north-south crustal thickness difference as follows:

$$\Delta D_{cr}^{\text{gra}} = D_{cr}^{S} - D_{cr}^{N} = a_{\text{dich}} \left(\frac{\rho_{cr}}{\rho_{m} - \rho_{cr}} \right) + b_{\text{dich}}, \tag{27}$$

with a slope $a_{\rm dich} = 3.447$ km and a y-intercept $b_{\rm dich} = 2.858$ km. The mean of the dichotomy is given by Equation 27. As for the standard deviation, we could use the standard deviation calculated from the linear regression, which is ± 0.1 km. This value is very small, and leaves little margin for our thermal model. We therefore use a standard deviation of ± 2 km, which is close to the numerical step used for the resolution of the temperature profile in the lid.

4.4.2. Average Thermal Lithosphere Thickness

The total conductive layer thickness is the sum of the lid thickness D_l and the thickness of the thermal boundary layer at the top of the convective mantle δ_u , $\left(D_L^{\rm calc} = D_l + \delta_u\right)$; we define it as the thermal lithosphere thickness. This lithosphere thickness is not a lithological boundary but a thermal boundary and is thus not easy to detect with seismological data. The conductive layer thickness is defined by the change in slope in the temperature profile between a conductive gradient and an isentropic gradient. On Mars, because of the low Martian gravity, the large temperature increase in the conductive lithosphere tends to decrease seismic waves velocities and may dominate over the effect of pressure, in particular for S-waves, more sensitive to temperature. The base of the thermal lithosphere on Mars may thus also correspond to a low-velocity zone for seismic waves. Arrival-time analysis of different seismic phases from a set of low-frequency marsquakes suggests a seismic velocity structure for the upper mantle that is compatible with the presence of a weak low-velocity zone corresponding to a thick lithosphere of 400–600 km (Khan et al., 2021). The more recent study of Durán et al. (2022) proposes a mean value of

BONNET GIBET ET AL. 15 of 31

450 km, with no associated standard deviation. We thus use a mean lithosphere thickness value of 450 km with a standard deviation of ± 100 km, as suggested by the range 400–600 km obtained in Khan et al. (2021):

$$D_L^{\text{avg}} = 450 \pm 100 \text{ km}.$$
 (28)

In our thermal evolution model, the present-day average thickness of the lid is calculated from a volume-weighted average of both hemispheres.

4.4.3. Present-Day Thermal State of the Martian Mantle

The mantle potential temperature is the projection to the planet's surface of the temperature at the top of the convective mantle T_m along the isentropic temperature gradient across the conductive layer thickness:

$$T_p^{\text{calc}} = T_m - \frac{\alpha g T_m}{c_m} D_L. \tag{29}$$

The olivine to wadsleyite phase transition causes a seismic discontinuity associated to a travel-time triplication. Huang et al. (2022) constrained the depth of this triplication to 1006 ± 40 km in the Martian mantle. The associated mantle temperature is estimated between 1,670 and 1892 K at the depth of the phase transition, accounting for uncertainties in the mantle composition. This temperature, projected along the isentropic gradient up to the Martian surface, provides a range for the present-day mantle potential temperature:

$$T_p = 1605 \pm 100 \text{ K},$$
 (30)

where the standard deviation includes uncertainties in depth and mantle mineralogy. Our model forecast is calculated from Equation 29 using the average thermal lithosphere thickness.

4.5. Monte Carlo - Markov Chain (MCMC) Algorithm

To approximate the posterior distribution, we implement a Markov chain and a Monte Carlo sampling algorithm (Sambridge et al., 2013). This sampling method performs a random walk through the parameter space, starting with a model \mathbf{m}_1 with N_p parameters to which we apply a small, random, perturbation to obtain a model \mathbf{m}_2 :

$$\mathbf{m}_2 = \mathbf{r}_a^{\text{gauss}}(\mathbf{m}_1, \boldsymbol{\sigma}_{\text{pertub}}), \tag{31}$$

where $\mathbf{r}_a^{\text{gauss}}$ is a vector of N_p random numbers following a Gaussian distribution centered around the \mathbf{m}_1 -parameters with a standard deviation $\boldsymbol{\sigma}_{\text{pertub}}$, where a given value for the standard deviation is defined for each parameter of our model (Table 3). We calculate the prior probability $p(\mathbf{m}_2)$ following the guidelines defined in Section 4.2. We then calculate the posterior probability of our two sets of model parameters which depends on the likelihood and the prior. We accept the new model \mathbf{m}_2 in our Markov chain if the following condition is verified:

$$\frac{p(\mathbf{m}_2|\mathbf{d})}{p(\mathbf{m}_1|\mathbf{d})} > \mathbf{r}_b \equiv \frac{p(\mathbf{d}|\mathbf{m}_2)p(\mathbf{m}_2)}{p(\mathbf{d}|\mathbf{m}_1)p(\mathbf{m}_1)} > \mathbf{r}_b, \tag{32}$$

where \mathbf{r}_b is a random number chosen uniformly between 0 and 1. If this condition is met, the model \mathbf{m}_2 is accepted, otherwise the model \mathbf{m}_1 is accepted again. The algorithm then restarts from the accepted model (\mathbf{m}_1 or \mathbf{m}_2), now called \mathbf{m}_1 to which we again apply a perturbation. This operation is repeated a sufficient number of times to sample the entire parameter space. The accepted models form a Markov chain which have the following properties: the distribution of the sampled model in this chain is equivalent to the model posterior distribution $p(\mathbf{m}|\mathbf{d})$. We can then approximate the posterior probability function of our model in the parameter space by calculating the density function of this collection of models. The acceptance rate measures the ratio of accepted over proposed models. This rate increases if we reduce the amplitude of the perturbations and decreases if we increase them. The optimal acceptance rate defined by statistics is around 44% (G. O. Roberts & Rosenthal, 2009).

BONNET GIBET ET AL. 16 of 31

4.6. Initial Thermal State

The temperature at the top of the convective mantle T_m^0 and the lithosphere thickness D_l^0 are set initially. Both are chosen such that the mantle is at the rheological transition to a solid-like convection 4.5 billion years ago, which allows the extraction of buoyant melts to form the crust (Lejeune & Richet, 1995; Scott & Kohlstedt, 2006). We define the rheological transition such that the maximum melt fraction within the mantle is equal to 0.35, which corresponds to an average melt fraction over the partially molten layer $\phi_a^{\rm N/S}$ of \sim 0.16. This initial condition on the melt fraction was not considered in Bonnet Gibet et al. (2022) where the initial mantle temperature and the initial viscosity evolved independently. For the crust, we start with an initial thickness of 4 km, for numerical reasons, and a classical crustal enrichment in heat-producing elements of 10 (Thiriet et al., 2018). We impose a small initial thermal perturbation to the symmetrical base state to trigger the instability in crustal growth; it consists in a small north-south difference in lid thickness ΔD_l^0 (Table 3), equivalent to a small north-south difference in heat flux.

4.7. Initial Phase

A preliminary exploration phase is necessary to the inversion. A series of inversions are first carried out with different perturbation values for each of the parameters (vector $\sigma_{perturb}$, Table 3) to find the perturbation amplitudes leading to an acceptance as close as possible to the optimal value of 44%. Once the parameters of the random walk are defined, we need to determine the necessary number of accepted models, that is, the length of the Markov chain, to ensure a good coverage of the parameter space. One way to determine the length of the chain is to perform an inversion without constraints on the data, that is, an inversion where the probability of the data likelihood $p(\mathbf{d}|\mathbf{m})$ is equal to 1; the posterior distribution should then be equal to the prior distribution. From a Markov chain with 1 million models, uniform distributions are reached, so this is the minimum number of models to gather for our inversions. The second purpose of this inversion with no observational constraints is to provide the prior distributions of the outputs of our thermal evolution model, including the forecasts. It is then possible to compare them to the posterior distributions of the outputs obtained when constraints on the data are accounted for in the inversion to evaluate whether observational data brings valuable constraints.

5. Results of the Inversion on Crustal Melting

5.1. Model Sets

Following this preliminary phase, an inversion is performed based on our 4 forecasts. 960 independent Markov chains are run in parallel starting from an identical model. The first 500 models collected for each channel are not accounted for in the final distribution, a phase known as burn-in: the algorithm takes a certain number of iterations to find the high-probability parameter space it has to sample. The ensemble of models obtained from each chain are summed to obtain a final ensemble solution with a total number of $N_{\rm asym} = 6.60 \times 10^6$ models whose acceptance rate is 42.54%, that is, close to the optimal value of 44%. We are interested in the proportion of models that are able to sustain partial melting at the base of the crust, which corresponds to thermal evolutions where the average maximum crustal melt fraction is non-zero. The proportion of models with a non-zero maximum melt fraction in the southern crust is 19.14%; it is 1.20% in the northern one. Partial melting of the southern crust is thus significant and an order of magnitude more likely than in the north. The proportion of models with crustal melting in the south but not in the north is 17.94%, which is exactly the difference between the two previous percentages. Hence, crustal melting in the north is only possible if the southern crust partially melts as well. We define a subset of models showing sustained crustal melting in the Southern Hemisphere but not in the Northern one. This subset represents $N_{\rm MELT} = 1.18 \times 10^6$ models, or 17.94% of the total number of models. This specific ensemble of models can be described as points in the 11-dimension parameter space (one dimension for each inverted parameter, Table 3).

5.2. Posterior Distribution of the Inverted Parameters

The distribution in parameter space formed by the subset of models with a crustal melting episode only in the south (red histograms, Figure 7) diverges significantly from the posterior distribution obtained for all models (blue curves, Figure 7). The 2D marginal distributions for the subset with crustal melting highlight covariances between parameters which help explain the emergence of crustal melting (colored graphs, Figure 7).

BONNET GIBET ET AL. 17 of 31

21699100, 2025, 3, Downloaded from https://agupubs.onlinelibrary.wiley.com/doi/10.1029/2024JE008486 by Dtsch Zentrum F. Luft-U. Raum Fahrt In D. Helmholtz Gemein., Wiley Online Library on [06/102025], See the Terms and Conditions (https://onlinelibrary.wiley.com/doi/10.1029/2024JE008486 by Dtsch Zentrum F. Luft-U. Raum Fahrt In D. Helmholtz Gemein., Wiley Online Library on [06/102025], See the Terms and Conditions (https://onlinelibrary.wiley.com/doi/10.1029/2024JE008486 by Dtsch Zentrum F. Luft-U. Raum Fahrt In D. Helmholtz Gemein., Wiley Online Library on [06/102025], See the Terms and Conditions (https://onlinelibrary.wiley.com/doi/10.1029/2024JE008486 by Dtsch Zentrum F. Luft-U. Raum Fahrt In D. Helmholtz Gemein., Wiley Online Library on [06/102025], See the Terms and Conditions (https://onlinelibrary.wiley.com/doi/10.1029/2024JE008486 by Dtsch Zentrum F. Luft-U. Raum Fahrt In D. Helmholtz Gemein., Wiley Online Library on [06/102025], See the Terms and Conditions (https://onlinelibrary.wiley.com/doi/10.1029/2024JE008486 by Dtsch Zentrum F. Luft-U. Raum Fahrt In D. Helmholtz Gemein., Wiley Online Library on [06/102025], See the Terms and Conditions (https://onlinelibrary.wiley.com/doi/10.1029/2024JE008486 by Dtsch Zentrum F. Luft-U. Raum Fahrt In D. Helmholtz Gemein., Wiley Online Library on [06/102025], See the Terms and Conditions (https://onlinelibrary.wiley.com/doi/10.1029/20.1029).

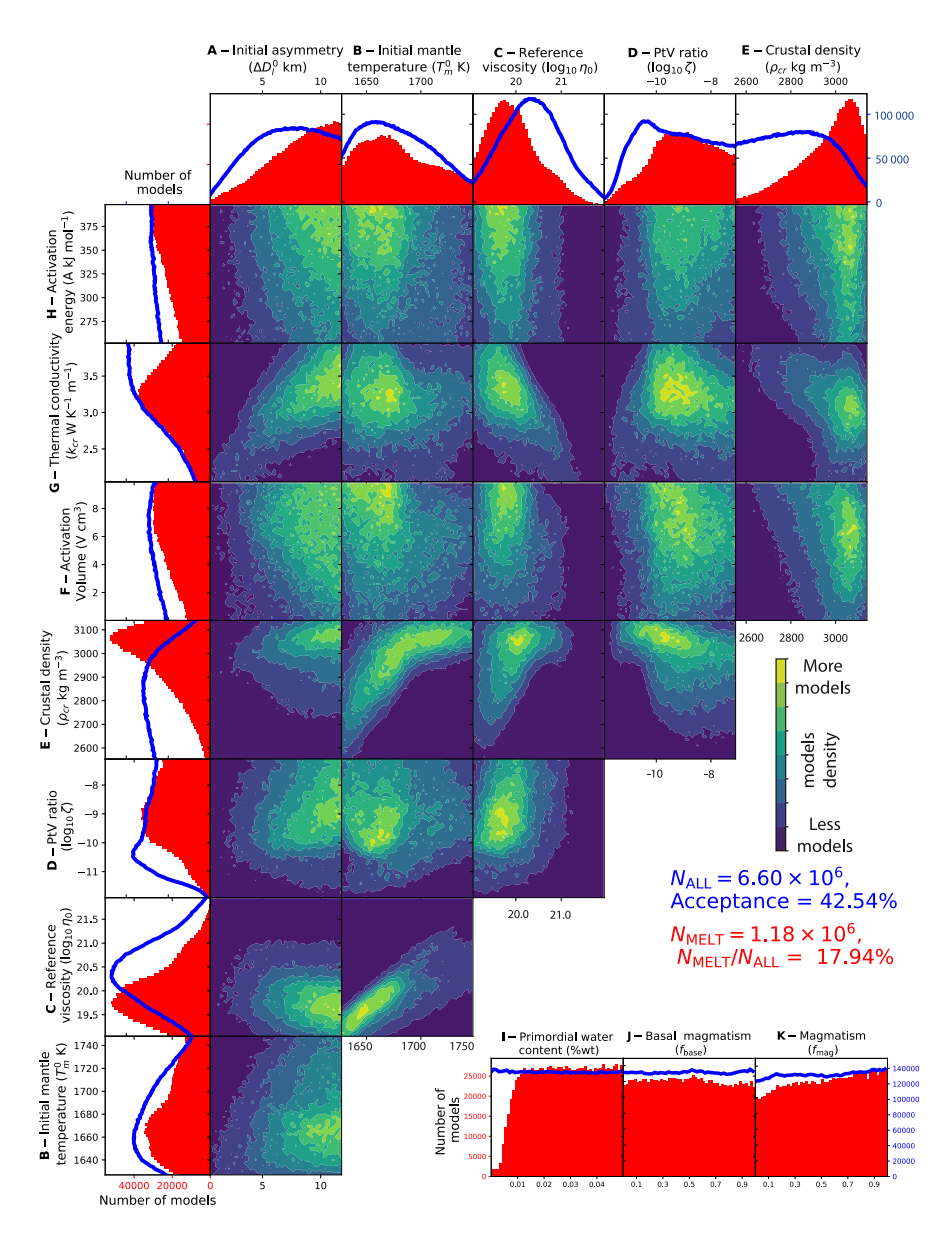


Figure 7. Projection along different inverted parameters of the probability distribution of our model, that is, 1D and 2D marginal distributions. Red histograms and 2D marginal distributions between the row and column parameters (with a dark blue to yellow colored scale) are for the subset of $N_{\rm MELT}$ models with crustal melting in the south. This subset represents 17.94% of the total number of models fitting our 4 constraints. The thick blue curves are the histogram envelopes representing the 1D marginal distributions for the full set of models fitting all constraints. (a) Initial perturbation in lid thickness (km), (b) initial temperature at the top of the convective mantle, (c) mantle reference viscosity (log scale), (d) Permeability to melt viscosity ratio, that is, PtV ratio (log scale), (e) crust density (kg m⁻³), (f) activation energy, (kJ mol⁻¹), (g) crust thermal conductivity (W m⁻¹ K⁻¹), (h) activation volume (cm³), (i) primitive mantle water content (wt% H₂O), (j) fraction of magmatism, (k) fraction of basal magmatism.

We obtain a Gaussian distribution for the reference viscosity with a rather low average of 2.3×10^{20} Pa s (Figure 7c, blue and Table 4): a low viscosity is required to reach a low present-day potential temperature. The reference viscosity in the subset with crustal melting (Figure 7c, red and Table 4) is shifted toward even smaller values with an average of 9.12×10^{19} Pa s. Lower viscosity leads to thinner lids and thicker crusts, hence to stronger temperature gradients and hotter temperatures at the base of the crust, favoring crustal melting. The inversion points to rather cold initial mantle temperatures ($\sim 1,680$ K) in both sets (Figure 7b and Table 4). The strong positive correlation between the initial mantle temperature and the reference viscosity (Figures 7b–7c) is

BONNET GIBET ET AL. 18 of 31

Set name		All inverted Models $6.60 \times 10^6 \text{ 42.54}\%$		Models with partial melting only in the southern crust $1.18 \times 10^6 17.94\%$	
Number of models acceptance					
Description	Parameter	Average	Standard deviation	Average	Standard deviation
Model parameters					
Reference viscosity	$\log_{10}\eta_0$	20.37	0.63	19.96	0.56
PtV ratio	$\log_{10} \zeta$	-9.292	1.247	-9.016	1.144
Initial mantle temperature	T_m^0 (K)	1,679	32	1,680	33
Crustal density	$\rho_{cr} (\mathrm{kg} \; \mathrm{m}^{-3})$	2,823	156	2,960	135
Crustal thermal conductivity	$k_{cr} ({\rm W} {\rm m}^{-1} {\rm K}^{-1})$	3.247	0.497	3.138	0.478
Activation energy	$A (kJ mol^{-1})$	327.4	43.0	334.5	42.1
Activation volume	V (cm ³)	5.236	2.812	5.682	2.702
Magmatism fraction	$f_{ m mag}$	0.507	0.289	0.522	0.287
Basal magmatism fraction	$f_{ m base}$	0.501	0.289	0.496	0.287
Primordial mantle water content	$X_{\mathrm{H}_{2}\mathrm{O}}^{p}$ (%wt)	0.025	0.014	0.028	0.013
Initial perturbation	ΔD_l^0 (km)	7.106	2.885	8.048	2.727
Model outputs					
Potential temperature	T_p (K)	1,635	66	1,582	52
Thermal lithosphere thickness	$D_{\rm L}$ (km)	424.4	51.3	416.9	49.5
InSight crust thickness	D_{InS} (km)	43.49	4.90	45.34	4.44
Average crust thickness	$D_{cr}^{\rm avg}$ (km)	58.78	7.14	65.63	6.58
Dichotomy amplitude	ΔD_{cr} (km)	20.72	7.41	27.63	8.64
Internal heating in the crust	$F_{ m HPE}^{cr}~(\%)$	54.38	6.52	58.78	7.75
CMB temperature	T_c (K)	1,874	72	1,821	61
Temperature gradient at R_l	$\frac{dT}{dz_{R_t}}$ (K km ⁻¹)	2.491	0.328	2.333	0.332
Temperature gradient at R_{cr}	$\frac{dT}{dz}_{R_{cr}} (\text{K km}^{-1})$	4.081	0.239	3.920	0.252

Note. Related distributions are shown in Figures 7 and 8.

induced by the choice of our initial state: the reference viscosity increases with the initial temperature to maintain a sufficiently thin initial lid thickness to result in an initial mantle fraction characteristic of the rheological transition.

The distribution of the amplitude of the initial thermal perturbation in the global set (Figure 7a, blue and Table 4) shows that there exists an optimal perturbation around 8 km for this parameter. Stronger initial perturbations produce dichotomies of larger amplitudes, which do not match with observations. Below 8 km, it is more difficult for the dichotomy to grow to expected amplitude. The subset of models with crustal melting in the south covers the upper range of initial perturbations because large initial perturbations trigger rapid formation of large dichotomies, more favorable to crustal melting (Figure 7a, red and Table 4). If a parameter value is tuned such that it favors dichotomy growth (such as a large initial thermal perturbation), the values of the other parameters also influencing on its growth, such as the crust thermal conductivity, must be adjusted to limit it such that it fits observational data.

For the global set, large crustal thermal conductivities are favored, though solutions are found for all values. The distribution in the subset with crustal melting is Gaussian-like with a maximum at \sim 3.2 W m⁻¹ K⁻¹ (Figure 7g). It is shifted toward lower values compared to the global set because the lower the thermal conductivity, the larger the growth of the dichotomy and the warmer the temperature at the base of the crust is. The combination of these two effects strongly favors melting at the base of the southern crust. Dichotomy growth is favored by smaller

BONNET GIBET ET AL. 19 of 31

crustal conductivities, as a higher thermal conductivity favors heat diffusion which dampens the positive feedback mechanism leading to dichotomy growth (Bonnet Gibet et al., 2022). Higher crustal thermal conductivities thus correlate with larger initial perturbations (Figures 7a–7g).

Similarly, in the subset with crustal melting, the activation volume decreases as the initial perturbation increases (Figures 7a–7f). The pressure-dependence of the viscosity leads indeed to another positive feedback between lid thickness and lid thickening (Watson et al., 2022), which tends to amplify the feedback between crust thickness and crust extraction and the growth of the dichotomy (Bonnet Gibet et al., 2022). The activation volume is on average higher in the subset with crustal melting than in the global case (Figure 7f) because larger activation volumes result in lower viscosities at low pressure (Bonnet Gibet et al., 2022), leading to thinner lids which promotes crust melting.

The average value of the permeability to melt viscosity ratio, or PtV ratio (Figure 7d, blue line), is 10^{-9} m² Pa⁻¹ s⁻¹ in the global set, which shows a distribution skewed toward low values. The distribution shows a maximum for PtV ratios between $\sim 10^{-10}$ and $\sim 10^{-9}$ m² Pa⁻¹ s⁻¹. PtV ratios lower than 10^{-9} m² Pa⁻¹ s⁻¹ are less frequent in the subset with crustal melting than for all models (Figure 7d, red histogram) because they imply a prolonged and delayed crustal extraction occurring on thicker, colder lids, less favorable to crustal melting. These low PtV ratios induce long extraction times which are more favorable to dichotomy growth (Bonnet Gibet et al., 2022) and hence favor low initial perturbations (Figures 7a–7d). High PtV ratios (> 10^{-9} m² Pa⁻¹ s⁻¹) result in large crustal extraction rates and rapid crust growth on a thin lithosphere, more favorable to crustal melting.

Larger viscosities and warmer initial mantle temperatures tend to generate thicker crusts and larger dichotomy amplitudes, as they lead to slower cooling and prolonged crustal extraction timescales. Stronger initial asymmetries ΔD_l^0 thus tend to be compensated by lower initial mantle temperatures and reference viscosities (Figures 7a–7c). For the same reasons, the reference viscosity correlates negatively with the crust thermal conductivity and positively with the PtV ratio (Figures 7c, 7d and 7g) while the PtV ratio correlates negatively with the crust thermal conductivity (Figures 7d–7g).

The crustal density is a proxy for the average crustal thickness and dichotomy amplitude (Section 4.4, Figures 5 and 6); it is relatively well constrained by the inversion (Figure 7e). The global set of accepted models shows a Gaussian distribution centered around ~2,820 kg m⁻³ (Table 4). The average crustal density is larger in the subset with crustal melting (Figure 7e), red and (Table 4). Larger crustal density values lead to thicker crusts and larger north-south differences in crustal thickness, which maximize the southern crustal thickness and favor melting at the base of the crust. Interestingly, the 2D marginal distribution for crustal density and other parameters influencing dichotomy growth tend to be bimodal. Parameter values impeding dichotomy growth (lower initial temperatures and reference viscosities, higher crust thermal conductivities and smaller PtV ratios) are associated with a distribution in crustal density that is similar to the global set of models, with a peak density around 2,900 kg m⁻³ (Figure 7e). On the contrary, parameter values favoring a prolonged and larger growth of the dichotomy are associated with large crustal densities of 3,000–3,100 kg m⁻³ (Figure 7e). Larger dichotomies are also favored by larger initial asymmetries; and, as expected, the crustal density tends to correlate positively with the initial perturbation (Figures 7a–7e).

The activation energy is not well constrained by the inversion in the global set (Figure 7h). The subset of models with crustal melting tends to slightly favor larger activation energy values (Figure 7h, red) because they result in hotter temperatures at the base of the lid (Davaille & Jaupart, 1993; Thiriet et al., 2019). The water content of the primordial mantle only affects the crustal solidus temperature, its distribution is thus constant for the global set of models and does not differ from the prior (Figure 7i, blue). The posterior water content distribution is constant above 100 ppm in the subset with crustal melting, but drops sharply below this value (Figure 7i, red). If the water content of the primitive mantle is larger, more water can be stored in the crust and the saturated solidus is more easily reached in the crust.

In both sets, the distribution of the fraction of basal magmatism does not differ significantly from the prior uniform distribution (Figure 7j). The distribution of the fraction of magmatism f_{mag} (Figure 7k, blue) increases very slightly toward 1 in the global set. In the subset with crustal melting, larger fractions of magmatism are slightly favored as they result in larger crustal temperature gradients (Figure 7k, red).

BONNET GIBET ET AL. 20 of 31

21699100, 2025, 3, Downloaded from https://agupubs.onlinelibrary.wiley.com/doi/10.1029/2024JE008486 by Disch Zentrum F. Luft-U. Raum Fahrt In D. Helimholtz Gemein.

Wiley Online Library on [06/10/2025]. See the Terms and Conditions (https://onlinelibrary.

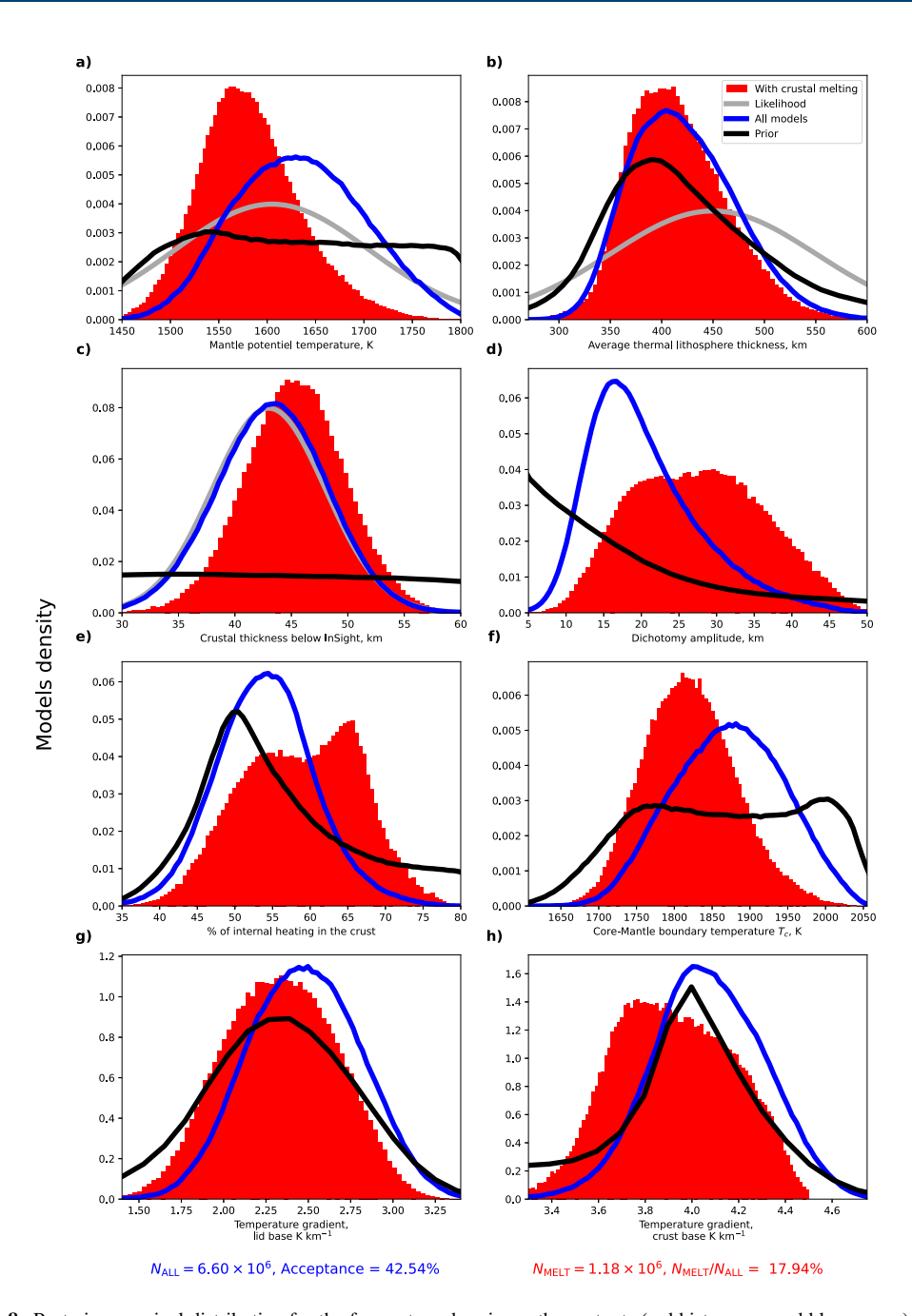


Figure 8. Posterior marginal distribution for the forecasts and various other outputs (red histograms and blue curves) compared to their prior distributions (black curves) and the likelihood for observational data (gray curves, as defined in Section 4.3). The red histograms represent the distribution for the subset of $N_{\rm MELT}$ models with crustal melting in the south which represent 17.94% of the total inverted models. Blue curves represent histogram envelopes for all $N_{\rm ALL}$ models. (a) Present-day mantle potential temperature (K), (b) present-day average lid thickness (km), (c) present-day crustal thickness below InSight, Equation 25 (km), (d) present-day dichotomy in crustal thickness (km), (e) percentage of the bulk radioactive heating present in the crust (% of total), (f) present-day temperature at the core-mantle boundary (K), (g) present-day average temperature gradient at the base of the crust (K km⁻¹).

5.3. Posterior Distribution of the Present-Day Thermal State

The posterior distribution of the current structure of Mars provides information on how the inversion enables to recover our constraints. Comparing the distributions obtained after inversion for the forecasts (blue curves and red

BONNET GIBET ET AL. 21 of 31



histograms on Figures 8a–8c) with the expected distribution from the observations ("likelihood," gray curves) as well as with the prior distributions, that are obtained without accounting for observations (black curves), demonstrates that, among our four observational data, crustal thickness data are clearly the most constraining data of our inversion.

The prior distribution of the mantle potential temperature covers a broad range of temperatures (Figure 8a black curve). Although in the expected range, both outcomes diverge from the distribution that we were aiming for (gray line, Equation 30), demonstrating that our inversion has better constrained the value of the mantle potential temperature than its expected range thanks to other observational data.

The likelihood for the thermal lithosphere thickness is more spread-out than our prior distribution (compare gray and black lines on Figure 8b). This means that our considerations on the lithosphere thickness (Equation 6) does not constrain our thermal evolution scenarios. Such values for the lithosphere thickness are in fact expected, and similar distributions between the global set and the subset with crustal melting are then obtained (Figure 8b and Table 4).

Our inversion corresponds very well to the expected crustal thickness below InSight (i.e., to the likelihood), both for the global set of models and the subset showing crustal melting (Figure 8c and Table 4). The gain in information thanks to our inversion compared to the prior is evident: the prior distribution spreads over a wide range of values from -15 km to +161 km, negative thicknesses below Insight being mathematically possible from Equation 25, for thin crusts and large crustal densities but are not physically realistic. Crustal melting is favored by larger crustal thicknesses, in the south in particular; the average thickness of the distribution is thus slightly higher in the subset of models with crustal melting (65.63 \pm 6.58 km) than for the global set (58.78 \pm 7.14 km), see Table 4. Similarly, the amplitude of the crustal dichotomy tends to be larger in the subset showing crustal melting than in the global set (Figure 8d).

Crustal melting is also favored by lower reference viscosities (Figure 7c), which induces thinner top thermal boundary layers early in the planet evolution, and hence larger temperature gradients more favorable to crustal melting. Lower reference viscosities tend to induce a colder present-day thermal state for Mars: the mantle potential temperature and the CMB temperature both peak toward colder values for the subset of models with crustal melting than for the global case (Figure 8a, red histogram and Table 4). Present-day temperature gradients at the base of the lid and crust are also shifted to lower values for the subset of models with crustal melting because of the colder present-day thermal states induced by lower viscosity values (Figure 8h and Table 4). Note that present-day temperature gradients tend to be lower at the lid base than at the crust base, indicating a significant change in temperature gradient within the lithospheric mantle (Figures 8g and 8h, blue curves).

The subset of models with crust melting tend to be associated to bimodal distributions for both the model parameters and the model outputs. This is most visible in the distribution of the percentage of internal heating in the crust: the first peak is similar to the global set, \sim 54%, while the second peaks at higher values of \sim 67% (Figure 8e). This is also visible, although less clearly, in the dichotomy amplitude and the temperature gradient at the crust base (Figures 8d–8h). These two modes correspond to crustal melting occurring either in relatively thin crusts, with low dichotomy amplitudes, or in very thick crusts with large dichotomy amplitudes, as described in previous Section 5.2 about the 2D marginal distribution of the crustal density.

5.4. Crustal Melting Output

Model outputs concerning the characteristics of crustal melting clearly show that the bimodal distributions of the different model parameters and outputs are linked to the two possible phases of crustal melting described in Section 5.2 and Figure 7.

Crustal melting is obtained for average crustal thicknesses that are generally thicker than in the global set of models. This average thickness is 65 km, against 58 km for the global set (Figure 9i and Table 4), but this single value conceals again a bimodal distribution, with a first peak at ~62 km, closer to the average of the global set, and a second, more significant, peak at ~67 km. A bimodal distribution is particularly evident in the ages associated to crustal melting (start and end age of melting): a very early peak is observed for both these ages (<300 Myr, Figures 9a and 9b). This represents a short and early melting episode that corresponds to the first phase of crustal melting presented in the thermal evolution example (Figure 4). These cases correlate with crustal thicknesses between 50 and 70 km (Figure 4). The second peak (~1 Gyr, Figures 9a and 9b) represents a late and longer

BONNET GIBET ET AL. 22 of 31

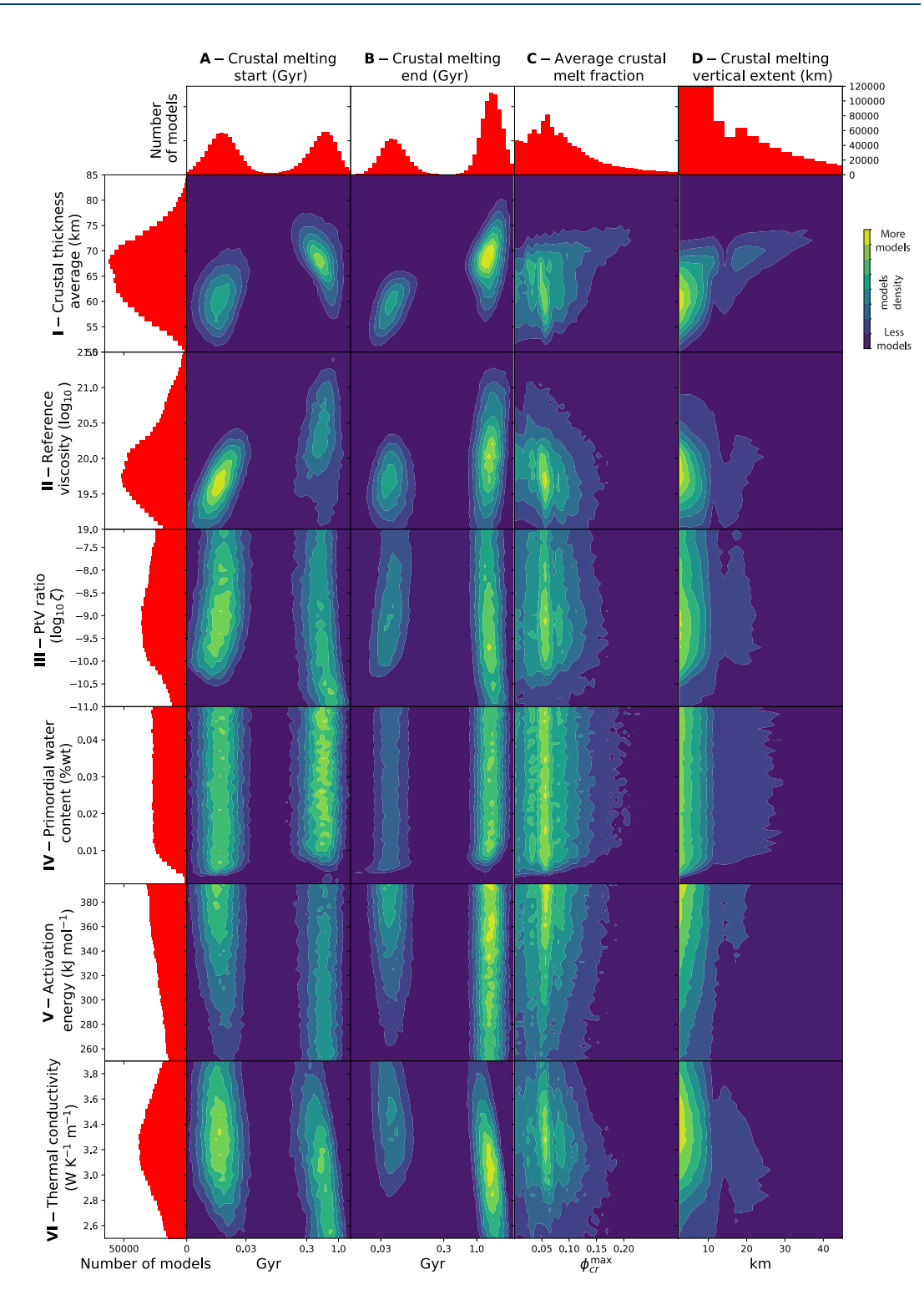


Figure 9. Posterior marginal distribution of different model outputs. Red histograms represent distributions for the subset of $N_{\rm MELT}$ models with crustal melting which represent 17.94% of the total of inverted models. (a) Age of the onset of crustal melting in the south (in Gyr represented on log scale to highlight the bimodal distribution), (b) age of the end of crustal melting in the south (Gyr, log scale), (c) maximum average melt fraction in the southern crust, (d) maximum thickness of the molten layer in the southern crust (km), (I average crustal thickness, II) reference viscosity of the mantle (log scale), (III) Permeability to melt viscosity ratio, that is, PtV ratio (log scale), (IV) primitive mantle water content (wt% H₂O), (V) activation energy, (kJ mol⁻¹), (VI) thermal conductivity of the crust (W m⁻¹ K⁻¹). Graphs in colored scale represent 2D marginal distributions between the row and column parameters, where the maximum density is in yellow and the minimum in purple.

BONNET GIBET ET AL. 23 of 31

crustal melting episode that corresponds to the second phase of crustal melting in the example of Figure 4. Models with a late and prolonged melting correlate with thicker crustal thicknesses of 60–80 km.

Models with crustal melting may show either only one or both of these melting episodes. Typically, for crustal thicknesses between 60 and 70 km, both crustal melting episodes coexist. For average crustal thicknesses less than 50 km, the crust does not melt.

Models characterized by an early and brief episode of crustal melting are associated with particularly low viscosities ($\lesssim 10^{20}$ Pa s, Figures 9a and 9b-II) and relatively large PtV ratio $\gtrsim 10^{-10}$ m² Pa⁻¹ s⁻¹ (Figures 9a and 9b-III). In this case, crustal extraction is rapid, but the lid grows slowly, resulting in very hot temperatures at the base of the crust. These temperatures exceed the solidus even in the anhydrous case, which explains the lack of dependence on the bulk water content (Figures 9a and 9b-IV). These models are also characterized by large activation energies inducing higher temperatures at the lid base.

For models with a late episode of crustal melting, the crust mostly forms later, when the lid is colder. In this case, the temperature at the crust base does not reach the solidus if the crust is dry and the bulk water content must be larger than 100 ppm for partial melting to occur in the crust (Figures 9a and 9b-IV). These late melting models cover a wider range of values for the reference viscosity, PtV ratio, activation energy and crust thermal conductivity and therefore different thermal evolution scenarios (Figures 9a, 9b-II, III, V, and VI). Lower PtV ratios, higher viscosities and lower crust thermal conductivities tend to prolong crustal melting (Figures 9a and 9b-II–VI).

The melt fraction averaged over the partially molten layer in the southern crust range from 0 to $\sim 30\%$ at the peak of the melting episode, with an average of 9.3% and a maximum probability at $\sim 5\%$ -6% (Figure 9c). The thickness of the partially molten layer in the crust range from 0 to a few tens of kilometres with an average of 15 km (Figure 9d); with thinner partially molten layers more likely than thicker ones. Cases with a molten thickness of ~ 10 km and a melt fraction of 5% on average are the most common.

The melt fraction and thickness of the partially molten layer tend to increase with the crustal thickness (Figures 9c-I and 9d-I). The molten thickness is \sim 5–10 km for crustal thicknesses up to 70 km. Above this value, the molten thickness and melt fraction can increase significantly. For some models, more than a third of the crustal thickness can be partially molten.

To summarize, cases showing crustal melting in the south are characterized by thick crusts, particularly in the south, and by a cold present-day initial state caused by a low reference viscosity (that favors early thin lithospheres and large temperature gradients in the lid and crust) and by a significant extraction of heat-producing elements from the mantle. The crust in the south can be partially molten over a thickness of a few to a few tens of kilometres. This melt fraction can also be significant (more than 10% Figure 8) and could produce rather large volumes of evolved melts. Crustal melting can either start very early in the thermal history of Mars (–4.5 Gyr ago) or much later (–3.8 Gyr ago) and over a variable duration (from tens of Myr to >1 Gyr). However, these values could be modified if we were accounting for the extraction of differentiated melts that would cause cooling at depth.

6. Discussion

6.1. Insights From Our Bayesian Inversion

6.1.1. A Present-Day Cold Martian Mantle

Our inversion points to a cold present-day thermal state for Mars, which is not surprising as we use seismological constraints suggesting a cold Martian mantle (Huang et al., 2022) with a thick lid (Drilleau et al., 2022; Durán et al., 2022; Khan et al., 2021). However, the most constraining observations for the present-day thermal state of Mars consist of the crustal thickness data. The potential temperature of the mantle and lid thickness are both estimated with a significantly smaller dispersion after our inversion than initial observations (Table 4). This cold thermal state implies a low reference viscosity and a large mantle depletion in heat-producing elements (Table 4). If we consider only models with crustal melting in the south, the resulting thermal state is even colder as even lower viscosity values are preferred.

BONNET GIBET ET AL. 24 of 31

The temperature gradient at the base of the lid is estimated between 1.5 and 3.25 K km⁻¹, in agreement with geophysical inversions (Drilleau et al., 2022; Durán et al., 2022; Khan et al., 2021). However, the gradient increases from the base of the lithosphere to the base of the crust, where it is between 3.4 and 4.5 K km⁻¹. Since the temperature gradient in the lid has a significant influence on the ray path and wave travel time, it seems important to account for its variation in the lid in travel-time inversions as in Drilleau et al. (2021, 2022, 2024).

6.1.2. Crustal Thickness Constraints on Mars' Thermal Evolution

Constraints on crustal thickness are more restrictive for the inversion than constraints on the mantle thermal state. The thermal evolution of Mars is indeed very dependent on the amount of crust and heat producing elements extracted from the mantle. Improving constraints on the thickness and density of the Martian crust could thus further improve our knowledge on the thermal evolution of Mars. Recent examples include constraints brought by the detection of Rayleigh waves for Marsquake S1222a. From the great circle path of these waves and crustal thickness maps, Kim et al. (2023) deduced a range of values for the average crustal thickness between 42 and 56 km. Such values, on the lower range of the one proposed initially by Knapmeyer-Endrun et al. (2021), would not favor crustal melting in the south. However, more recently, Drilleau et al. (2024) constrained lateral variations in crustal thickness using body wave arrival times combined with topography and gravity field modeling. Their results point to a crustal thickness below InSight of ~45 km and to an average thickness of ~66 km, that is, in that case, on the upper end of previous estimates. Such values would, inversely, favor the emergence of crustal melting during crust construction.

6.1.3. Water Content of the Primitive Mantle

Our inversion shows that a minimum of ~ 100 ppm of water in the bulk silicate is required for crustal melting in the south (Figure 7i). In our thermal evolution model, water only plays on the crustal solidus; its effect on mantle rheology and dynamics is not accounted for. In the literature, estimates of the bulk silicate water content span several orders of magnitude, from 1 ppm (Mysen et al., 1998) to 1,000 ppm (Johnson et al., 1991). Estimates come from the study of SNC meteorites and are based on geochemical models. Geodynamical estimates rely on the effect of water on mantle rheology, searching for the rheology, among dry or wet olivine, that best explains the planet dynamics. For early Mars, a wet rheology has been proposed to explain the thermal evolution (Hauck & Phillips, 2002), elastic thickness estimates (Thiriet et al., 2018) and relaxation of the dichotomy (Guest & Smrekar, 2005), which, according to G. J. Taylor (2013), would correspond to a water content of 600 ppm. Our inversion results converge toward a low reference viscosity ($\sim 10^{20}$ Pa s, Figure 8c) which could correspond to an intermediate rheology, between wet and dry olivine (Karato & Wu, 1993). But the presence of water is not the only factor that could induce a more ductile rheology in the past: the presence of melt also causes a reduction in the bulk viscosity (Breuer & Spohn, 2006). Mei et al. (2002) proposes an exponential reduction in viscosity with increasing melt fraction. However, this reduction only affects the partially molten upper layer that makes a small fraction of the total mantle volume. It is thus not entirely clear how the reduction in viscosity caused by the presence of melt affects the dynamics of the whole mantle. Samuel et al. (2019) use a viscosity depending on the melt rheology, which increases the convective heat flux. Not surprisingly, their results point to a much higher reference viscosity, as it is then reduced by the presence of melt. Thus it is not clear whether this low viscosity points to an early water-rich or partially molten mantle (or both).

Dehydration stiffening of a water-rich mantle associated to crustal extraction might act to thicken the lid by underplating of the rigid and buoyant mantle residue. This could have a significant impact on mantle dynamics (Fraeman & Korenaga, 2010; Plesa & Breuer, 2014; Zhong, 2009) and would play against the mechanism we propose. However, such a rheological wet-to-dry transition might not be efficient if the mantle water content is below 300 ppm, the concentration at which this transition takes place (Korenaga & Karato, 2008). Additionnally, the change in residue density, driven by an increase in Mg# by crustal extraction, is likely smaller in the iron-rich Martian mantle compared to Earth's. Collinet et al. (2015) estimate that the Mg# increases from 75–77 to 77–79 after 15–25% of melting, which amounts to a change in Mg# of \sim 0.02 per melt percent for a typical Martian mantle, while it is \sim 0.08 for the Earth (Kinzler & Grove, 1992; Korenaga, 2006).

BONNET GIBET ET AL. 25 of 31

6.1.4. Origin of the Dichotomy

Our inversion demonstrates that the positive feedback mechanism we identified in Bonnet Gibet et al. (2022) is able to generate the observed dichotomy from an initially small perturbation in lid thickness (0.5–12 km. Figure 7a) over a very wide range of parameters (Figure 8d) within the parameter space needed to account for the thermal structure observed by InSight. The average initial perturbation in lid thickness from the inversion is ~7 km for the global set (Figure 7a). Solutions exist over the full range by either amplifying or dampening the perturbation through the effects of other model parameters influencing the positive feedback. Considering an initial lid thickness of 50 km and a temperature jump of 1300 K in the lid, a hemispheric difference in lid thickness of 7 km corresponds to a difference in heat flux of ~15 mW m⁻² which represents 14.5% of the initial heat flux (i.e., 104 mW m⁻²). In terms of temperature, a difference in lid thickness of 7 km between the two hemispheres would represent a temperature difference of 91 K at the average depth of the lid base. Whether a finite hemispherical perturbation is first required, or not, to trigger the growth of our mechanism can thus be debated. But this inversion, which tests the sensitivity of our thermal evolution model to the initial perturbation, shows that, after reaching a peak at ~8 km, the probability decreases. We therefore expect that strong initial hemispherical perturbations are less likely to generate the expected dichotomy, all the more if we consider a perturbation in crustal thickness, the effect of which is considerably larger than that of a difference in lid thickness (Bonnet Gibet et al., 2022). It has been suggested that the dichotomy could form as a results of an early giant impact in the north (Marinova et al., 2008, 2011) or in the south (Ballantyne et al., 2023; Cheng et al., 2024; Golabek et al., 2011; Leone et al., 2014; Reese et al., 2010). However, a challenge for the impact models lies in achieving reasonable crustal thicknesses in the impacted hemisphere (Cheng et al., 2024; Marinova et al., 2011). A giant impact generates an initially strong crustal thickness dichotomy, which would further grow through the positive feedback mechanism we highlight. In contrast, an initial temperature or heat flux anomaly caused by a short episod of degree-1 convection (J. H. Roberts & Zhong, 2006; Šrámek & Zhong, 2012) resulting from a rheologically layered mantle or inherited from the magma ocean (Morison et al., 2019; Watson et al., 2022) is more consistent with our results because the associated temperature anomalies are close to those inferred from our inversion (~90 K, J. H. Roberts & Zhong, 2006). After the initial degree-one instability has formed, our feedback mechanism does not require its persistence to create the dichotomy. Finally, the full range of initial perturbations can lead to crustal melting in the Southern Hemisphere. But crustal melting would be more likely if the initial perturbation is not infinitesimal and if our feedback mechanism was triggered by an endogenic degree-one mechanism.

6.2. Partial Melting of the Crust and Differentiation of the Southern Highlands

6.2.1. Hemispheric Scale

Partial melting of the crust at the scale of the Southern Hemisphere is a likely event during Mars' thermal evolution: crustal melting occurs in the Southern Hemisphere in a substantial part (17.94%) of the models fitting InSight constraints that emerge from our inversion. The growth of a strong hemispheric dichotomy, caused by the positive feedback mechanism we identify, provides the conditions for melting in the south where the crust is thicker. A thick crust allows not only for higher temperatures but also for lower melting temperatures, as more water can dissolve into the melt at higher pressures, lowering the solidus. The lower thermal conductivities of crustal rocks also cause larger temperature gradients, favoring crust melting. Similarly, lower mantle reference viscosities also favor crustal melting because (a) it leads to thinner lids, larger melt fractions and larger crusts, and (b) the lid is thinner, and its temperature gradient is larger when the crust forms. A water content of 100 ppm in the primordial mantle is sufficient to achieve crustal melting in all cases. On the other hand, heating by magmatism does not seem to significantly modify the temperature gradient in the crust, as the heat deposited compensates for the cooling caused by downward advection of material underneath.

However, although crustal melting at the scale of the Southern Hemisphere is possible, it appears limited and cannot affect more than a third of the crust thickness. Partial melting of the crust on a hemispherical scale, with a maximum vertical extent of 30 km and 10% melt fraction, would produce a layer of more felsic rocks of \sim 3 km thick at most. These buoyant melts would rise to shallower depths. But, given the large thickness of the crust in the southern hemisphere and the slow ascent rate caused by a low density contrast, a large fraction would likely crystallize at depth. This process may have resulted in the formation of an intermediate layer of undifferentiated basalt mixed with some more differentiated rocks. Thus, it does not appear possible to generate a layered crust

BONNET GIBET ET AL. 26 of 31

with an upper differentiated layer overlying an intermediate basaltic layer and a deep layer formed by mafic residues on a hemispherical scale, as suggested by McCubbin et al. (2008), through this mechanism. In addition, these felsic rocks could then be covered by subsequent mafic lavas (Payré et al., 2022, 2024).

6.2.2. Timing for Crustal Melting

Episodes of sustained partial melting in the crust can take place at two specific periods. The first period occurs very early, between 4.5 and 4.3 billion years ago, which corresponds to the age of zircons found in NWA 7034 meteorite (Cassata et al., 2018) and to age estimates proposed for the province Terra Cimmeria/Sirenum (Bouley et al., 2020). During this early and short crustal melting episode, less than \sim 10 km of crust can partially melt (Figure 8). A second episode of crustal melting can occur toward the end of crustal formation, between 4 and 3 billion years ago and for \sim 1 Gyr. The maximum amplitude of melting is reached when the crust completes its formation at \sim 3.5 Gyr, that is, during the Hesperian. This period would thus be suitable for the production of magma over a prolonged duration. There is evidence of significant explosive volcanism in the highlands at that time (Brož et al., 2021). Explosive volcanism is characteristic of magma enriched in volatiles, particularly water. On Mars, explosive volcanoes can be fed by basaltic magmas enriched in volatiles through their interaction with underground water (Carr, 1979); they could also come from crustal differentiation in presence of water.

6.2.3. Terra Cimmeria-Sirenum: A Continental Crust Under Formation?

The thickness of the crust is not uniform in the highlands, and there are strong variations in between provinces. A small increase in crustal thickness, over a sufficiently large province, can lead to a significant increase in the crustal melt fraction and in the thickness of the partially molten layer through the increase in basal temperature and the decrease in solidus temperature (Section 2.4, Figure 3). Models where melting on a hemispherical scale is limited could locally lead to larger volumes of differentiated magma. Thermal evolutions where melting is not reached on a hemispherical scale could also sustain limited crustal melting in thick crustal provinces. As a significant proportion of these differentiated melts may crystallize at depths; they could constitute a barrier to the ascent of denser melts and prevent the resurfacing of the province. Terra Sirenum/Cimmeria is a good candidate for this scenario: it is a geological province characterized by a very thick crust (Figure 1 and Bouley et al. (2020)) and feldspar-rich outcrops (Payré et al., 2022). It may be the region of origin of NWA 7034, and it is bounded by the Gusey and Gale craters, where differentiated rocks have been observed. Zircon ages in the NWA 7034 breccia are between 4.42 and 4.47 Gyr (Cassata et al., 2018) and are compatible with an early and rapid melting of the crust. The assimilation and fractional crystallisation model proposed by Ostwald et al. (2022), which accurately reproduces the alkaline suite composition observed in Gale Crater (Cousin et al., 2017; Sautter et al., 2015, 2016), aligns closely with our proposed model. Both scenarios involve the formation of mafic magma from partial melting of the primitive mantle, followed by slow cooling within the crust that facilitates fractional crystallisation and crustal assimilation, modifying the magma composition. In the preferred models of Ostwald et al. (2022), felsic rocks form at pressures of 2-6 kbar, corresponding to depths of 20-60 km, which fits to our model's melting depths during the first melting event (Figure 4d).

Sautter et al. (2015) suggested that the presence and composition of differentiated rocks found in Gale crater could indicate the presence of a continental crust on Mars. This raises the question of the extent to which the Terra Cimmeria/Sirenum province fits this description. The Earth's continental crust is characterized by rocks richer in silica than the basaltic oceanic crust. The majority (\sim 60%) of rocks forming the continental crust belong to the TTG series (Tonalite-Trondhjemite-Granodiorite, Rudnick & Holland, 2005). These rocks were likely produced by partial melting of a hydrated basaltic crust in thick crustal provinces (Jaupart et al., 2018; Sizova et al., 2015). Felsic samples described by Sautter et al. (2015) are petrologically quite similar to these TTGs. However, Udry et al. (2018) argue that their chemistry better corresponds to Icelandic rocks than to TTGs. From a geodynamic point of view, the continental crust is characterized by a low density, allowing it to "float" at the surface (S. R. Taylor & McLennan, 2009). Considering our scenario for the evolution of the Terra Cimmeria/Sirenum province, the region may be composed of differentiated rocks, basalts and mafic residues at the base of the crust. Differentiated rocks are less dense than basalt, but mafic residues, that are much more voluminous, are denser. Hence, the total density of the crust changes little by the process of differentiation and cannot by itself generate a lowdensity crust. On Earth, in absence of orogen, the maximum thickness of the continental crust is ~40 km (Laske et al., 2013). This, together with the rather low continental crust density, is explained by the loss of dense mafic residues, that become dynamically unstable, because denser than the mantle at pressures characteristics of the

BONNET GIBET ET AL. 27 of 31

base of the Earth's crust (Jull & Kelemen, 2001). These dense mafic residues could sink back to the mantle as the lithosphere was not strong enough to hold them (Jaupart et al., 2018). By losing these mafic roots, the bulk density of the continental crust is then largely reduced. In our study, we demonstrated that dense mafic residues could form in thick crustal regions on Mars through crustal differentiation and extraction of evolved melts, forming a low-density upper crustal component. The overall density of the crust is then not modified by this process as we do not model the loss of mafic residues, and this is consistent with our assumption of a uniform density for the crust (Section 4.4). Whether these mafic residues could in fact be lost is an open question. Gravity data being more sensitive to shallower layers, the low densities found in the highlands may be more representative of the upper layers of the crust than of its bulk properties and does not provide any evidence for the loss of mafic residues (Goossens et al., 2017; Pauer & Breuer, 2008). Since lid thickening is rapid on a small planet like Mars, which prevents crustal recycling, differentiation would have to occur very early for mafic residues to be recycled in the convective mantle, which may be possible, as shown in this study (Figure 8).

7. Conclusion

We investigated the possibility that differentiated rocks observed in the Martian highlands were formed during crust construction, by fractional crystallisation of a basaltic crust. To enable fractional crystallisation, part of the crust must be maintained above its solidus temperature so that magma can evolve in composition before being extracted to form differentiated rocks. We show that this is possible at the base of the Martian highlands, at the scale of a hemisphere, and given the constraints we have on Mars' crustal thickness. Thicker crusts lead to higher temperatures at the Moho. Pressures characteristics of the base of thick crusts on Mars also enable a significant quantity of water to be dissolved in the melt which significantly reduces the solidus. We demonstrate that the combined effects of hotter temperatures and a lower solidus, together with a rather weak mantle rheology, allow to sustain partial melting and crustal differentiation over geological times in the Southern Hemisphere. Using our thermal evolution model in a Bayesian inversion scheme with constraints on Mars' crustal structure and present-day thermal state, we find that partial melting of the southern crust during its construction is a non-negligible possibility. Partial melting of the crust may occur early and over a short duration, or later and over a prolonged duration. Crustal differentiation can thus occur in absence of plate tectonics, but seems limited in vertical extent to a fraction of the crustal thickness. Whether the loss of mafic residues could occur and generate a low density crust remains an open question.

Data Availability Statement

The source code (C++) used to produce the data is available in Bonnet Gibet (2024a). Figures can be fully reproduced using the post-processing codes and data referenced in Bonnet Gibet (2024b).

References

Agee, C. B., Wilson, N. V., McCubbin, F. M., Ziegler, K., Polyak, V. J., Sharp, Z. D., et al. (2013). Unique meteorite from early Amazonian Mars: Water-rich basaltic breccia Northwest Africa 7034. Science, 339(6121), 780–785. https://doi.org/10.1126/science.1228858

Andrews-Hanna, J. C., Zuber, M. T., & Banerdt, W. B. (2008). The Borealis basin and the origin of the Martian crustal dichotomy. *Nature*, 453(7199), 1212–1215. https://doi.org/10.1038/nature07011

Atherton, M. P., & Petford, N. (1993). Generation of sodium-rich magmas from newly underplated basaltic crust. *Nature*, 362(6416), 144–146. https://doi.org/10.1038/362144a0

Aubaud, C., Hauri, E. H., & Hirschmann, M. M. (2004). Hydrogen partition coefficients between nominally anhydrous minerals and basaltic melts. Geophysical Research Letters, 31(20). https://doi.org/10.1029/2004GL021341

Ballantyne, H. A., Jutzi, M., Golabek, G. J., Mishra, L., Cheng, K. W., Rozel, A. B., & Tackley, P. J. (2023). Investigating the feasibility of an impact-induced Martian Dichotomy. *Icarus*, 392, 115395. https://doi.org/10.1016/j.icarus.2022.115395

Bandfield, J. L. (2006). Extended surface exposures of granitoid compositions in Syrtis Major, Mars. Geophysical Research Letters, 33(6). https://doi.org/10.1029/2005GL025559

Baratoux, D., Samuel, H., Michaut, C., Toplis, M. J., Monnereau, M., Wieczorek, M., et al. (2014). Petrological constraints on the density of the Martian crust. *Journal of Geophysical Research: Planets*, 119(7), 1707–1727. https://doi.org/10.1002/2014je004642

Barthez, M., Flahaut, J., Guitreau, M., Ito, G., & Pik, R. (2023). Understanding VNIR plagioclase signatures on Mars through petrographic, geochemical, and spectral characterization of terrestrial feldspar-bearing igneous rocks. *Journal of Geophysical Research: Planets*, 128(8). https://doi.org/10.1029/2022JE007680

Batra, K., & Foley, B. (2021). Scaling laws for stagnant-lid convection with a buoyant crust. *Geophysical Journal International*, 228(1), 631–663. https://doi.org/10.1093/gji/ggab366

Bayes, T. (1763). LII. An essay towards solving a problem in the doctrine of chances. By the late rev. Mr. Bayes, FRS communicated by Mr. Price, in a letter to John Canton, Amfr S. *Philosophical Transactions of the Royal Society of London*(53), 370–418.

Black, B., & Marchi, S. (2024). Buoyant impact partial melts on ancient mars. *Journal of Geophysical Research: Planets*, 129(1). https://doi.org/10.1029/2023JE008040

Acknowledgments

The authors thank Bradford Foley and two anonymous reviewers for their helpful comments on the manuscript. This project has received funding from the European Research Council under the European Union's Horizon 2020 research and innovation programme (Grant 101001689). CM acknowledges support from the Institut Universitaire de France. VBG and CM acknowledge the French Space Agency CNES and ANR (MAGIS ANR-19-CE31-0008-08) for funding the InSight Science analysis. This is InSight contribution 349.

BONNET GIBET ET AL. 28 of 31

- Bonnet Gibet, V. (2024a). 1PIECE—1D-Planetary- interior-evolution-with-crust-extration: 1PIECE Version v0 [Software]. https://doi.org/10.5281/zenodo.13796565
- Bonnet Gibet, V. (2024b). Martian highlands differentiation concomitant to Dichotomy Formation Data & Software [Dataset]. Zenodo. https://doi.org/10.5281/zenodo.13913464
- Bonnet Gibet, V., Michaut, C., Wieczorek, M., & Lognonné, P. (2022). A positive feedback between crustal thickness and melt extraction for the origin of the Martian dichotomy. *Journal of Geophysical Research: Planets*, 127(12). https://doi.org/10.1029/2022JE007472
- Bouley, S., Keane, J. T., Baratoux, D., Langlais, B., Matsuyama, I., Costard, F., et al. (2020). A thick crustal block revealed by reconstructions of early Mars Highlands. *Nature Geoscience*, 13(2), 105–109. https://doi.org/10.1038/s41561-019-0512-6
- Breuer, D., & Spohn, T. (2003). Early plate tectonics versus single-plate tectonics on Mars: Evidence from magnetic field history and crust evolution. *Journal of Geophysical Research*, 108(E7). https://doi.org/10.1029/2002JE001999
- Breuer, D., & Spohn, T. (2006). Viscosity of the Martian mantle and its initial temperature: Constraints from crust formation history and the evolution of the magnetic field. *Planetary and Space Science*, 54(2), 153–169. https://doi.org/10.1016/j.pss.2005.08.008
- Brož, P., Bernhardt, H., Conway, S. J., & Parekh, R. (2021). An overview of explosive volcanism on Mars. *Journal of Volcanology and Geothermal Research*, 409, 107125. https://doi.org/10.1016/j.jvolgeores.2020.107125
- Carr, M. H. (1979). Formation of Martian flood features by release of water from confined aquifers. *Journal of Geophysical Research: Solid Earth*, 84(B6), 2995–3007. https://doi.org/10.1029/jb084ib06p02995
- Carter, J., & Poulet, F. (2013). Ancient plutonic processes on Mars inferred from the detection of possible anorthositic terrains. *Nature Geoscience*, 6(12), 1008–1012. https://doi.org/10.1038/ngeo1995
- Cassata, W. S., Cohen, B. E., Mark, D. F., Trappitsch, R., Crow, C. A., Wimpenny, J., et al. (2018). Chronology of Martian breccia NWA 7034 and the formation of the Martian crustal dichotomy. *Science Advances*, 4(5), eaap8306. https://doi.org/10.1126/sciadv.aap8306
- Cheng, K. W., Ballantyne, H. A., Golabek, G. J., Jutzi, M., Rozel, A. B., & Tackley, P. J. (2024). Combined impact and interior evolution models in three dimensions indicate a southern impact origin of the Martian dichotomy. *Icarus*, 420, 116137. https://doi.org/10.1016/j.icarus.2024.
- Christensen, P., McSween Jr, H., Bandfield, J., Ruff, S., Rogers, A., Hamilton, V., et al. (2005). Evidence for magmatic evolution and diversity on Mars from infrared observations. *Nature*. 436(7050), 504–509. https://doi.org/10.1038/nature03639
- Collinet, M., Médard, E., Charlier, B., Vander Auwera, J., & Grove, T. L. (2015). Melting of the primitive Martian mantle at 0.5–2.2 GPa and the origin of basalts and alkaline rocks on Mars. Earth and Planetary Science Letters, 427, 83–94. https://doi.org/10.1016/j.epsl.2015.06.056
- Costa, M. M., Jensen, N. K., Bouvier, L. C., Connelly, J. N., Mikouchi, T., Horstwood, M. S., et al. (2020). The internal structure and geodynamics of Mars inferred from a 4.2-Gyr zircon record. *Proceedings of the National Academy of Sciences*, 117(49), 30973–30979. https://doi.org/10.1073/pnas.2016326117
- Cousin, A., Sautter, V., Payré, V., Forni, O., Mangold, N., Gasnault, O., et al. (2017). Classification of igneous rocks analyzed by ChemCam at Gale crater, Mars. *Icarus*, 288, 265–283. https://doi.org/10.1016/j.icarus.2017.01.014
- Davaille, A., & Jaupart, C. (1993). Transient high-Rayleigh-number thermal convection with large viscosity variations. *Journal of Fluid Mechanics*, 253(-1), 141–166. https://doi.org/10.1017/s0022112093001740
- Deschamps, F., & Sotin, C. (2001). Thermal convection in the outer shell of large icy satellites. *Journal of Geophysical Research*, 106(E3), 5107–5121. https://doi.org/10.1029/2000je001253
- Drilleau, M., Garcia, R., Samuel, H., Rivoldini, A., Wieczorek, M., Lognonné, P., et al. (2022). Marsquakes' location and 1-D seismic models for Mars from Insight data. *Journal of Geophysical Research: Planets*, 127(9). https://doi.org/10.1029/2021je007067
- Drilleau, M., Samuel, H., Garcia, R. F., Rivoldini, A., Perrin, C., Wieczorek, M., et al. (2024). Constraints on lateral variations of Martian crustal thickness from seismological and gravity field measurements. Geophysical Research Letters, 51(4). https://doi.org/10.1029/2023GL105701
- Drilleau, M., Samuel, H., Rivoldini, A., Panning, M., & Lognonné, P. (2021). Bayesian inversion of the Martian structure using geodynamic constraints. *Geophysical Journal International*, 226(3), 1615–1644. https://doi.org/10.1093/gji/ggab105
- Durán, C., Khan, A., Ceylan, S., Zenhäusern, G., Stähler, S., Clinton, J., & Giardini, D. (2022). Seismology on Mars: An analysis of direct, reflected, and converted seismic body waves with implications for interior structure. *Physics of the Earth and Planetary Interiors*, 325, 106851. https://doi.org/10.1016/j.pepi.2022.106851
- Elkins-Tanton, L. T. (2012). Magma oceans in the inner solar system. Annual Review of Earth and Planetary Sciences, 40(1), 113–139. https://doi.org/10.1146/annurev-earth-042711-105503
- Elkins-Tanton, L. T., Parmentier, E., & Hess, P. (2003). Magma ocean fractional crystallization and cumulate overturn in terrestrial planets: Implications for Mars. *Meteoritics & Planetary Sciences*, 38(12), 1753–1771. https://doi.org/10.1111/j.1945-5100.2003.tb00013.x
- Flahaut, J., Payet, V., Fueten, F., Guitreau, M., Barthez, M., Ito, G., & Allemand, P. (2023). New detections of feldspar-bearing volcanic rocks in the walls of Valles Marineris, Mars. *Geophysical Research Letters*, 50(2). https://doi.org/10.1029/2022GL100772
- Foley, B. J., & Smye, A. J. (2018). Carbon cycling and habitability of Earth-sized stagnant lid planets. Astrobiology, 18(7), 873–896. https://doi.org/10.1089/ast.2017.1695
- Fraeman, A. A., & Korenaga, J. (2010). The influence of mantle melting on the evolution of Mars. *Icarus*, 210(1), 43–57. https://doi.org/10.1016/j.icarus.2010.06.030
- Gallagher, K., Charvin, K., Nielsen, S., Sambridge, M., & Stephenson, J. (2009). Markov chain Monte Carlo (MCMC) sampling methods to determine optimal models, model resolution and model choice for Earth Science problems. *Marine and Petroleum Geology*, 26(4), 525–535. https://doi.org/10.1016/j.marpetgeo.2009.01.003
- Giordano, D., Russell, J. K., & Dingwell, D. B. (2008). Viscosity of magmatic liquids: A model. Earth and Planetary Science Letters, 271(1-4), 123–134. https://doi.org/10.1016/j.epsl.2008.03.038
- Golabek, G. J., Keller, T., Gerya, T. V., Zhu, G., Tackley, P. J., & Connolly, J. A. (2011). Origin of the Martian dichotomy and Tharsis from a giant impact causing massive magmatism. *Icarus*, 215(1), 346–357. https://doi.org/10.1016/j.icarus.2011.06.012
- Goossens, S., Sabaka, T. J., Genova, A., Mazarico, E., Nicholas, J. B., & Neumann, G. A. (2017). Evidence for a low bulk crustal density for Mars from gravity and topography. *Geophysical Research Letters*, 44(15), 7686–7694. https://doi.org/10.1002/2017gl074172
- Green, D. H., & Ringwood, A. (1967). An experimental investigation of the gabbro to eclogite transformation and its petrological applications. Geochimica et Cosmochimica Acta, 31(5), 767–833. https://doi.org/10.1016/s0016-7037(67)80031-0
- Guest, A., & Smrekar, S. E. (2005). Relaxation of the Martian dichotomy boundary: Faulting in the Ismenius region and constraints on the early evolution of Mars. *Journal of Geophysical Research*, 110(E12). https://doi.org/10.1029/2005JE002504
- Hauck, S. A., & Phillips, R. J. (2002). Thermal and crustal evolution of Mars. *Journal of Geophysical Research: Planets*, 107(E7), 6-1. https://doi.org/10.1029/2001JE001801
- Huang, Q., Schmerr, N. C., King, S. D., Kim, D., Rivoldini, A., Plesa, A.-C., et al. (2022). Seismic detection of a deep mantle discontinuity within Mars by Insight. *Proceedings of the National Academy of Sciences*, 119(42), e2204474119. https://doi.org/10.1073/pnas.2204474119

BONNET GIBET ET AL. 29 of 31

- Humayun, M., Nemchin, A., Zanda, B., Hewins, R., Grange, M., Kennedy, A., et al. (2013). Origin and age of the earliest Martian crust from meteorite NWA 7533. *Nature*, 503(7477), 513–516. https://doi.org/10.1038/nature12764
- Jaupart, C., Mareschal, J.-C., & Roman, A. (2018). The Formation of continental crust from a physics perspective. Geochemistry International, 56(13), 1289–1321. https://doi.org/10.1134/s0016702918130049
- Johnson, M. C., Rutherford, M. J., & Hess, P. C. (1991). Chassigny petrogenesis: Melt compositions, intensive parameters and water contents of Martian (?) magmas. Geochimica et Cosmochimica Acta, 55(1), 349–366. https://doi.org/10.1016/0016-7037(91)90423-3
- Joshi, R., Knapmeyer-Endrun, B., Mosegaard, K., Wieczorek, M. A., Igel, H., Christensen, U. R., & Lognonné, P. (2023). Joint Inversion of receiver functions and apparent incidence angles to determine the crustal structure of Mars. Geophysical Research Letters, 50(3). https://doi. org/10.1029/2022GL100469
- Jull, M., & Kelemen, P. á. (2001). On the conditions for lower crustal convective instability. Journal of Geophysical Research, 106(B4), 6423–6446. https://doi.org/10.1029/2000jb900357
- Karato, S.-i., & Wu, P. (1993). Rheology of the upper mantle: A synthesis. Science, 260(5109), 771–778. https://doi.org/10.1126/science.260. 5109.771
- Katz, R. F., Spiegelman, M., & Langmuir, C. H. (2003). A new parameterization of hydrous mantle melting. Geochemistry, Geophysics, Geosystems, 4(9). https://doi.org/10.1029/2002GC000433
- Khan, A., Ceylan, S., van Driel, M., Giardini, D., Lognonné, P., Samuel, H., et al. (2021). Upper mantle structure of Mars from Insight seismic data. *Science*, 373(6553), 434–438. https://doi.org/10.1126/science.abf2966
- Kim, D., Duran, C., Giardini, D., Plesa, A.-C., Stähler, S. C., Boehm, C., et al. (2023). Global crustal thickness revealed by surface waves orbiting Mars. Geophysical Research Letters, 50(12). https://doi.org/10.1029/2023GL103482
- Kinzler, R. J., & Grove, T. L. (1992). Primary magmas of mid-ocean ridge basalts 1. experiments and methods. *Journal of Geophysical Research*, 97(B5), 6885–6906. https://doi.org/10.1029/91jb02840
- Knapmeyer-Endrun, B., Panning, M. P., Bissig, F., Joshi, R., Khan, A., Kim, D., et al. (2021). Thickness and structure of the Martian crust from Insight seismic data. *Science*, 373(6553), 438–443. https://doi.org/10.1126/science.abf8966
- Korenaga, J. (2006). Archean geodynamics and the thermal evolution of Earth. Geophysical Monograph-American Geophysical Union, 164, 7–32. https://doi.org/10.1029/164gm03
- Korenaga, J., & Karato, S.-I. (2008). A new analysis of experimental data on olivine rheology. Journal of Geophysical Research, 113(B2). https://doi.org/10.1029/2007JB005100
- Lagain, A., Bouley, S., Zanda, B., Miljković, K., Rajšić, A., Baratoux, D., et al. (2022). Early crustal processes revealed by the ejection site of the oldest Martian meteorite. *Nature Communications*, 13(1), 3782. https://doi.org/10.1038/s41467-022-31444-8
- Laske, G., Masters, G., Ma, Z., & Pasyanos, M. (2013). Update on CRUST1. 0—A 1-degree global model of Earth's crust. In *Geophysical research abstracts* (Vol. 15(15), p. 2658).
- research abstracts (Vol. 15(15), p. 2658).
 Lejeune, A.-M., & Richet, P. (1995). Rheology of crystal-bearing silicate melts: An experimental study at high viscosities. *Journal of Geophysical*
- Research, 100(B3), 4215–4229. https://doi.org/10.1029/94JB02985 Leone, G., Tackley, P. J., Gerya, T. V., May, D. A., & Zhu, G. (2014). Three-dimensional simulations of the southern polar giant impact hy-
- pothesis for the origin of the Martian dichotomy. *Geophysical Research Letters*, 41(24), 8736–8743. https://doi.org/10.1002/2014g1062261 Lin, Y., Tronche, E. J., Steenstra, E. S., & van Westrenen, W. (2017). Evidence for an early wet moon from experimental crystallization of the lunar magma ocean. *Nature Geoscience*, 10(1), 14–18. https://doi.org/10.1038/ngeo2845
- Mangold, N., Loizeau, D., Poulet, F., Ansan, V., Baratoux, D., LeMouelic, S., et al. (2010). Mineralogy of recent volcanic plains in the Tharsis region, Mars, and implications for platy-ridged flow composition. *Earth and Planetary Science Letters*, 294(3–4), 440–450. https://doi.org/10.1016/j.epsl.2009.07.036
- Mareschal, J.-C., & Jaupart, C. (2006). Archean thermal regime and stabilization of the cratons. *Archean geodynamics and environments*, 164, 61–73. https://doi.org/10.1029/164gm06
- Marinova, M. M., Aharonson, O., & Asphaug, E. (2008). Mega-impact formation of the Mars hemispheric dichotomy. *Nature*, 453(7199), 1216–1219. https://doi.org/10.1038/nature07070
- Marinova, M. M., Aharonson, O., & Asphaug, E. (2011). Geophysical consequences of planetary-scale impacts into a Mars-like planet. *Icarus*, 211(2), 960–985. https://doi.org/10.1016/j.icarus.2010.10.032
- McCubbin, F. M., Nekvasil, H., Harrington, A. D., Elardo, S. M., & Lindsley, D. H. (2008). Compositional diversity and stratification of the Martian crust: Inferences from crystallization experiments on the picrobasalt Humphrey from Gusev crater, Mars. *Journal of Geophysical Research*, 113(E11). https://doi.org/10.1029/2008JE003165
- McKenzie, D. (1985). The extraction of magma from the crust and mantle. Earth and Planetary Science Letters, 74(1), 81–91. https://doi.org/10.1016/0012-821x(85)90168-2
- Mclennan, S. (2012). Geochemistry of sedimentary processes on Mars. Sedimentary Geology of Mars, 102, 119–138. https://doi.org/10.2110/pec. 12.102.0119
- Mei, S., Bai, W., Hiraga, T., & Kohlstedt, D. (2002). Influence of melt on the creep behavior of olivine–basalt aggregates under hydrous conditions. *Earth and Planetary Science Letters*, 201(3–4), 491–507. https://doi.org/10.1016/s0012-821x(02)00745-8
- Michalski, J. R., Deanne Rogers, A., Edwards, C. S., Cowart, A., & Xiao, L. (2024). Diverse volcanism and crustal recycling on early Mars. Nature Astronomy, 8(4), 456–462. https://doi.org/10.1038/s41550-023-02191-7
- Miller, K. J., Zhu, W.-l., Montési, L. G., & Gaetani, G. A. (2014). Experimental quantification of permeability of partially molten mantle rock. Earth and Planetary Science Letters, 388, 273–282. https://doi.org/10.1016/j.epsl.2013.12.003
- Morison, A., Labrosse, S., Deguen, R., & Alboussière, T. (2019). Timescale of overturn in a magma ocean cumulate. *Earth and Planetary Science Letters*, 516, 25–36. https://doi.org/10.1016/j.epsl.2019.03.037
- Morschhauser, A., Grott, M., & Breuer, D. (2011). Crustal recycling, mantle dehydration, and the thermal evolution of Mars. *Icarus*, 212(2), 541–558. https://doi.org/10.1016/j.icarus.2010.12.028
- $Mysen, B. O., Virgo, D., Popp, R. K., \& Bertka, C. M. (1998). The role of H_2O in Martian magmatic systems. \textit{American Mineralogist}, 83(9-10), 942-946. \\ https://doi.org/10.2138/am-1998-9-1002$
- Nyquist, L. E., Shih, C.-Y., McCubbin, F. M., Santos, A. R., Shearer, C. K., Peng, Z. X., et al. (2016). Rb-Sr and Sm-Nd isotopic and REE studies of igneous components in the bulk matrix domain of Martian breccia Northwest Africa 7034. *Meteoritics & Planetary Sciences*, 51(3), 483–498. https://doi.org/10.1111/maps.12606
- Ostwald, A., Udry, A., Payré, V., Gazel, E., & Wu, P. (2022). The role of assimilation and fractional crystallization in the evolution of the Mars crust. Earth and Planetary Science Letters, 585, 117514. https://doi.org/10.1016/j.epsl.2022.117514
- Pauer, M., & Breuer, D. (2008). Constraints on the maximum crustal density from gravity-topography modeling: Applications to the southern highlands of Mars. Earth and Planetary Science Letters, 276(3-4), 253–261. https://doi.org/10.1016/j.epsl.2008.09.014

BONNET GIBET ET AL. 30 of 31



Journal of Geophysical Research: Planets

- 10.1029/2024JE008486
- Payré, V., Salvatore, M., & Edwards, C. (2022). An evolved early crust exposed on Mars revealed through spectroscopy. *Geophysical Research Letters*, 49(21). https://doi.org/10.1029/2022GL099639
- Payré, V., Udry, A., & Fraeman, A. A. (2024). Igneous diversity of the early Martian crust. *Minerals*, 14(5), 452. https://doi.org/10.3390/min14050452
- Peacock, S. M., Rushmer, T., & Thompson, A. B. (1994). Partial melting of subducting oceanic crust. Earth and Planetary Science Letters, 121(1–2), 227–244. https://doi.org/10.1016/0012-821x(94)90042-6
- Phillips, M. S., Viviano, C. E., Moersch, J. E., Rogers, A. D., McSween, H. Y., & Seelos, F. P. (2022). Extensive and ancient feldspathic crust detected across north Hellas rim, Mars: Possible implications for primary crust formation. *Geology*, 50(10), 1182–1186. https://doi.org/10. 1130/e50341.1
- Plesa, A.-C., & Breuer, D. (2014). Partial melting in one-plate planets: Implications for thermo-chemical and atmospheric evolution. *Planetary and Space Science*, 98, 50–65. https://doi.org/10.1016/j.pss.2013.10.007
- Plesa, A.-C., Padovan, S., Tosi, N., Breuer, D., Grott, M., Wieczorek, M., et al. (2018). The thermal state and interior structure of mars. Geophysical Research Letters, 45(22), 12–198. https://doi.org/10.1029/2018g1080728
- Reese, C., Orth, C., & Solomatov, V. (2010). Impact origin for the Martian crustal dichotomy: Half emptied or half filled? *Journal of Geophysical Research*, 115(E5). https://doi.org/10.1029/2009JE003506
- Richter, F. M., & McKenzie, D. (1984). Dynamical models for melt segregation from a deformable matrix. *The Journal of Geology*, 92(6), 729–740. https://doi.org/10.1086/628908
- Roberts, G. O., & Rosenthal, J. S. (2009). Examples of adaptive MCMC. Journal of Computational & Graphical Statistics, 18(2), 349–367. https://doi.org/10.1198/icgs.2009.06134
- Roberts, J. H., & Zhong, S. (2006). Degree-1 convection in the Martian mantle and the origin of the hemispheric dichotomy. *Journal of Geophysical Research*, 111(E6). https://doi.org/10.1029/2005JE002668
- Rudnick, R. L., & Holland, H. D. (2005). Treatise on geochemistry. 3. The crust. Elsevier Pergamon.
- Sambridge, M., Bodin, T., Gallagher, K., & Tkalčić, H. (2013). Transdimensional inference in the geosciences. Philosophical Transactions of the Royal Society A: Mathematical, Physical & Engineering Sciences, 371(1984), 20110547. https://doi.org/10.1098/rsta.2011.0547
- Samuel, H., Lognonné, P., Panning, M., & Lainey, V. (2019). The rheology and thermal history of Mars revealed by the orbital evolution of Phobos. *Nature*, 569(7757), 523–527. https://doi.org/10.1038/s41586-019-1202-7
- Santos, A. R., Agee, C. B., McCubbin, F. M., Shearer, C. K., Burger, P. V., Tartèse, R., & Anand, M. (2015). Petrology of igneous clasts in Northwest Africa 7034: Implications for the petrologic diversity of the Martian crust. *Geochimica et Cosmochimica Acta*, 157, 56–85. https://doi.org/10.1016/j.gca.2015.02.023
- Sautter, V., Toplis, M., Wiens, R., Cousin, A., Fabre, C., Gasnault, O., et al. (2015). In situ evidence for continental crust on early Mars. *Nature Geoscience*, 8(8), 605–609. https://doi.org/10.1038/ngeo2474
- Sautter, V., Toplis, M. J., Beck, P., Mangold, N., Wiens, R., Pinet, P., et al. (2016). Magmatic complexity on early Mars as seen through a combination of orbital, in-situ and meteorite data. *Lithos*, 254, 36–52. https://doi.org/10.1016/j.lithos.2016.02.023
- Scott, T., & Kohlstedt, D. (2006). The effect of large melt fraction on the deformation behavior of peridotite. Earth and Planetary Science Letters, 246(3), 177–187. https://doi.org/10.1016/j.epsl.2006.04.027
- Sisson, T., & Kelemen, P. (2018). Near-solidus melts of MORB+ 4 wt% H₂O at 0.8–2.8 GPa applied to issues of subduction magmatism and continent formation. *Contributions to Mineralogy and Petrology*, 173(9), 1–23. https://doi.org/10.1007/s00410-018-1494-x
- Sizova, E., Gerya, T., Stüwe, K., & Brown, M. (2015). Generation of felsic crust in the archean: A geodynamic modeling perspective. *Precambrian Research*, 271, 198–224. https://doi.org/10.1016/j.precamres.2015.10.005
- Šrámek, O., & Zhong, S. (2012). Martian crustal dichotomy and Tharsis formation by partial melting coupled to early plume migration. *Journal of Geophysical Research*, 117(E1). https://doi.org/10.1029/2011je003867
- Taylor, G. J. (2013). The bulk composition of Mars. Geochemistry, 73(4), 401-420. https://doi.org/10.1016/j.chemer.2013.09.006
- Taylor, S. R., & McLennan, S. (2009). Planetary crusts: Their composition, origin and evolution (Vol. 10). Cambridge University Press. https://doi.org/10.1017/cbo9780511575358
- Thiriet, M., Breuer, D., Michaut, C., & Plesa, A.-C. (2019). Scaling laws of convection for cooling planets in a stagnant lid regime. *Physics of the Earth and Planetary Interiors*, 286, 138–153. https://doi.org/10.1016/j.pepi.2018.11.003
- Thiriet, M., Michaut, C., Breuer, D., & Plesa, A.-C. (2018). Hemispheric dichotomy in lithosphere thickness on Mars caused by differences in crustal structure and composition. *Journal of Geophysical Research: Planets*, 123(4), 823–848. https://doi.org/10.1002/2017je005431
- Turcotte, D. L., & Schubert, G. (2002). Geodynamics. Cambridge University Press.
 Udry, A., Gazel, E., & McSween Jr, H. Y. (2018). Formation of evolved rocks at Gale crater by crystal fractionation and implications for Mars crustal composition. Journal of Geophysical Research: Planets, 123(6), 1525–1540. https://doi.org/10.1029/2018je005602
- Watson, C., Neufeld, J. A., & Michaut, C. (2022). Early asymmetric growth of planetary stagnant lids. *Journal of Fluid Mechanics*, 952, A3. https://doi.org/10.1017/ifm.2022.864
- Wieczorek, M. A. (2015). Gravity and topography of the terrestrial planets. Treatise on geophysics, 10, 165–206. https://doi.org/10.1016/b978-044452748-6/00156-5
- Wieczorek, M. A., Broquet, A., McLennan, S. M., Rivoldini, A., Golombek, M., Antonangeli, D., et al. (2022). Insight constraints on the global character of the Martian crust. *Journal of Geophysical Research: Planets*. https://doi.org/10.1029/2022JE007298
- Wray, J. J., Hansen, S. T., Dufek, J., Swayze, G. A., Murchie, S. L., Seelos, F. P., et al. (2013). Prolonged magmatic activity on Mars inferred from the detection of felsic rocks. *Nature Geoscience*, 6(12), 1013–1017. https://doi.org/10.1038/ngeo1994
- Zhong, S. (2009). Migration of Tharsis volcanism on Mars caused by differential rotation of the lithosphere. *Nature Geoscience*, 2(1), 19–23. https://doi.org/10.1038/ngeo392

BONNET GIBET ET AL. 31 of 31